Pro Gradu

Development of an Inductive NIS Thermometer

Geng Zhuoran

January 23, 2012

UNIVERSITY OF JYVÄSKYLÄ
NANOSCIENCE CENTER
DEPARTMENT OF PHYSICS
NANOPHYSICS

SUPERVISOR: Ilari Maasilta

Preface

The work reported in this Master's thesis has been done between Jan 2010 and July 2011 at Nanoscience Center at the Department of Physics in the University of Jyväskylä.

First and foremost, I would like to thank my supervisor Professor Ilari Maasilta, who has given me excellent guidance both in the experimental and theoretical work as well as in writing process of this Master's thesis. In addition, I would like to thank him for the interesting research topic and the opportunity to work in his experimental nanophysics group. I would also like to thank Dr. Kimmo Kinnunen for his valuable contribution to all the experiments, especially with low temperature measurements. I would like to thank especially our present and former group members Dr. Saumyadip Chaudhuri, Dr. Panu Koppinen, Dr. Jenni Karvonen, Mr. Tero Isotalo, Mr. Mikko Palosaari, Ms. Minna Nevala, Mr. Juhani Julin, Mr. Andrii Torgovkin and Ms. Tian Yaolan for the valuable advices and helping me with the research. I also want to thank persons from outside our group for creating a good atmosphere in Nanoscience Center, especially our laboratory engineers Mr. Antti Nuottajärvi and Mr. Tarmo Suppula for their technical support.

I also wish to thank my friends, Mr. Shen Boxuan for his support and the wonderful times we spent together outside of physics. Finally, I am the most grateful to my beloved wife Tianbai for her love and support, and for standing by me and listening to my endless speech on physics.

Jyväskylä January 2012

Geng Zhuoran

Abstract

Normal metal-Insulator-Superconductor (NIS) tunnel junction thermometers have been under heavy research since 1976 after Rowell and Tsui first presented thanks to their excellent sensitivity to the temperature change in millikelvin regime. In this work, we have designed and studied an inductive readout for NIS tunnel junctions by using on-chip planar inductors and a DC SQUID (Superconducting Quantum Interference Device) to develop a sensitive and fast thermometer for studies of nanoscale heat conduction and bolometry.

In this thesis, the processing of the samples fabricated in Nanoscience Center in Jyväskylä are presented, and several processing challenges have been dealt with and the fabrication recipe is discussed in detail. Two measurements were performed on our sample, one with a normal DC measurement setup, and the other with a AC bias and SQUID read-out setup. Our initial results indicates that the SQUID measurement follows well the DC bias measurement and the BCS theory for the SINIS junction, and shows that it is feasible to use this scheme to directly measure the conductance of a SINIS device at audio frequencies with a good sensitivity for temperatures below 1 K for aluminum as the superconductor when voltage biased close to the superconductor energy gap.

Contents

Introduction

The desire for sensitive bolometers has encouraged people to develop fast response, low temperature and nanoscale normal metal-insulator-superconductor (NIS) tunnel junction thermometers, which can easily be integrated into antenna and absorber structures to form the bolometer [1–3]. Such a device has strongly temperature-dependent current-voltage characteristics, submicron size, low self heating and natural bandwidth up to few MHz [4], and has been used extensively in studies of low-temperature thermal transport [5–7]. It is also an attractive candidate for far-infrared bolometry applications [8].

However, in all previous applications the NIS thermometer is working under constant current bias, with a measurement of the temperature dependence of the voltage (or resistance) across the tunnel junction $V(T)$ [9]. In contrast, in this study we have fabricated a novel on-chip sub-Kelvin symmetric SINIS thermometer, which is biased with DC voltage and read out using four on-chip planar inductors to amplify and inductively couple the current signal to a DC SQUID mounted on the 1 K stage of the refrigerator. By using this method, we can measure the conductance and the temperature dependence of the conductance of the NIS tunnel junctions above the audio frequency range and pre-amplify the signal before the SQUID. It will give us the following potential benefits: (i) increased sensitivity due to the low-temperature preamplifier stage, (ii) increased read-out bandwidth, as capacitive loading of the wiring is reduced, and (iii) reduced external noise heating radiated down from the read-out circuit. This last issue is typically limiting the operational range of SINIS thermometers to > 100 mK if no strong measures are taken to filter the high-frequency noise.

Chapter 1

Theory and Background

1.1 Superconductivity

Superconductivity plays a very important role in this thesis, thus it will be introduced here with phenomena and a theory offering explanation.

Soon after H. Kamerlingh Onnes had first liquefied helium, he observed the phenomenon that the electrical resistance of mercury disappeared completely in a small temperature range at a critical temperature T_c, in 1911 in Leiden. [10–12] This phenomenon of superconductivity exists in many metals and alloys, which electrical resistivity drops suddenly to zero when they are cooled to sufficiently low temperature, for example in the range of boiling point of liquid helium (4.2 K). Thus *perfect conductivity* is the first traditional hallmark of superconductivity.

But a superconductor is more than an ideal conductor. The second hallmark that was discovered by Meissner and Ochsenfeld [13] in 1933 was *perfect diamagnetism*. They found that a superconductor will always expel magnetic field below T_c, regardless of whether there is a initial field inside it at normal state or not. This could certainly not be explained by *perfect conductivity*, which would tend to trap flux inside as it is cooled through T_c shown in Fig. 1.1.

From 1950s, the naturel of superconductivity is under extensive and careful study. It began in the 1948, when Fritz London proposed his famous phenomenological *London Equations* [15]. After rapid progress in the study and understanding of superconductivity, Bardeen, Cooper and Schrieffer assembled all evidence and results to construct a very accurate theoretical picture for the classical superconductors [16]. However, in 1986 a new type of su-

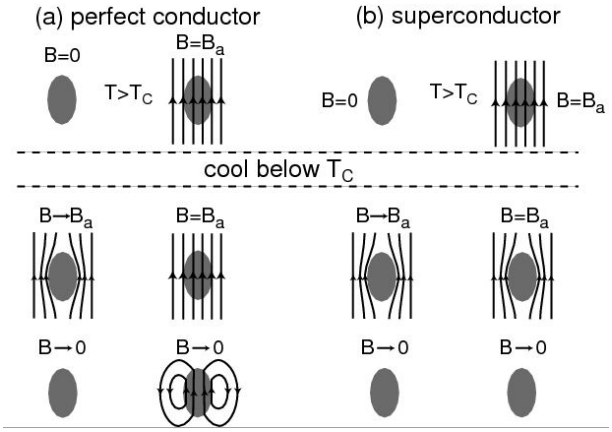

Figure 1.1: (a) shows the behavior of a *perfect conductivity*. For this material the magnetic field in the specimen below T_c depends on the presence and size of a magnetic field before cooling down below T_c. (b) shows the situation for a genuine superconductor which displays the *Meissner effect*. The interior of the specimen is field free below T_c, independent of the sample's history. Picture taken from Ref. [14]

perconductor, which has transition temperature (T_c) considerably above the previous limit of 30 K was discovered by Bednorz and Müller [17]. It is believed that at these temperatures other effects are at play beyond the BCS theory; these effects are not yet fully understood.

1.1.1 BCS Theory and the Energy Gap

In 1957, Bardeen, Cooper and Schrieffer (BCS) proposed a microscopic theory for the origins of superconductivity, which successfully predicts the properties of elemental superconductors, after Ginzburg-Landau suggested their macroscopic theory in 1950 [18].

The basic idea of BCS theory is that, a material can form a real ground state by pairs of bound electrons. These pairs are known as *Cooper pairs* and are formed by electron-phonon interactions. As shown in Fig. 1.2, an electron in the cation lattice will distort the ion cores around it, creating an area of greater positive charge density around itself (phonon). Another electron in the lattice nearby will then be attracted to this phonon as electron-phonon interaction. Thus this mechanism is teeming up electrons are indirectly attracted to each other instead of repulsed by the screened Coulomb interaction in superconductors. These Cooper pairs require a finite a mount of energy to

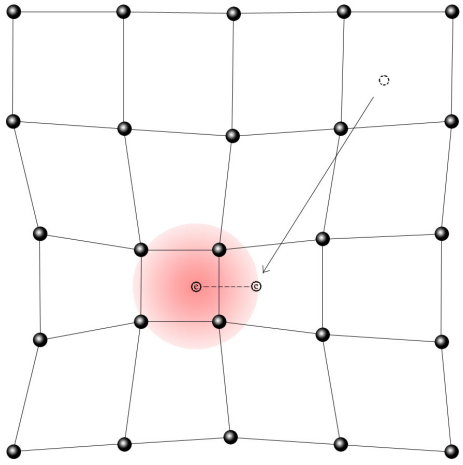

Figure 1.2: Cooper pair formation trough electron-phonon interaction: the electron is attracted to the positive charge density created by the first electron distroting the lattice around itself.

break and thus resistant to thermal vibrations below the critical temperature.

Temperature Dependence of the Energy Gap

one of the most important prediction from BCS theory is that in order to break a Cooper pair and form two quasi-particle excitations, a minimum energy $E_g = 2\Delta(T)$ is required. The theory estimates this energy gap at T=0 K as [19]:

$$E_g(0) = 2\Delta(0) = 3.528 k_B T_c, \tag{1.1}$$

where k_B is Bolzmann constant, $\Delta(0)$ is the gap per quasiparticle at $T = 0$.

This energy gap between the ground state and the quasi-particle excitations of the system determines many interesting electromagnetic properties of a superconductor. Also this gap value $\Delta(T)$ was predicted to increase from zero at T_c to the finite value given in Eq. 1.1 according to given in Ref. [19]:

$$\frac{1}{N(0)V} = \int_0^{\hbar\omega_c} \frac{d\epsilon}{\sqrt{\epsilon^2 + \Delta^2}} \tanh\left(\frac{\beta\sqrt{\epsilon^2 + \Delta^2}}{2}\right), \tag{1.2}$$

where $\beta = \frac{1}{k_B T}$, $N(0)$ is the density of states of Fermi surface in the normal state, and V describes the strength of the attractive interaction between electrons near the Fermi surface, and $\hbar\omega_c$ is the cutoff energy for this attractive

interaction, which is the Debye energy for phonon mediated attraction.

At $T = 0$, since $\beta \to \infty$, the master equation Eq. 1.2 can be written as:

$$\frac{1}{N(0)V} = \int_0^{\hbar\omega_c} \frac{d\epsilon}{\sqrt{\epsilon^2 + \Delta^2(0)}}. \tag{1.3}$$

At weak coupling limit ($\hbar\omega_c >> \Delta$), integration yields

$$\Delta(0) \cong 2\hbar\omega_c \exp\left(-\frac{1}{N(0)V}\right). \tag{1.4}$$

At $T = T_c$, since $\Delta(T_c) = 0$, the master equation can be written as:

$$\frac{1}{N(0)V} = \int_0^{\hbar\omega_c} \frac{\tanh(\beta_c\epsilon/2)d\epsilon}{\epsilon}, \tag{1.5}$$

and integration yields

$$k_B T_c = \frac{2\hbar\omega_c e^C}{\pi} \exp\left(-\frac{1}{N(0)V}\right), \tag{1.6}$$

where $C \cong 0.577$ is the Euler constant.

Comparing Eq. 1.4 and Eq. 1.6 gives:

$$\frac{2\Delta(0)}{k_B T_c} \cong 3.528, \tag{1.7}$$

which proves Eq. 1.1.

To calculate the temperature dependence of $\Delta(T)$, we use Eq. 1.5 and combine with the master equation Eq. 1.2:

$$\int_0^{\hbar\omega_c} \left[\frac{1}{\epsilon}\tanh\left(\frac{\beta_c\epsilon}{2}\right) - \frac{1}{\sqrt{\epsilon^2+\Delta^2}}\tanh\left(\frac{\beta\sqrt{\epsilon^2+\Delta^2}}{2}\right)\right] d\epsilon = 0. \tag{1.8}$$

If $\hbar\omega_c >> k_B T_c$ (weak coupling limit), a small error is made if we replace the upper limit in the integration to infinity:

$$\int_0^{\infty} \left[\frac{1}{\epsilon}\tanh\left(\frac{\beta_c\epsilon}{2}\right) - \frac{1}{\sqrt{\epsilon^2+\Delta^2}}\tanh\left(\frac{\beta\sqrt{\epsilon^2+\Delta^2}}{2}\right)\right] d\epsilon = 0. \tag{1.9}$$

Adding $\int_0^{\infty}(\tanh(\beta\epsilon/2)/\epsilon - \tanh(\beta\epsilon/2)/\epsilon) = 0$ in to Eq.1.9, we set

$$\int_0^{\infty} \left[\frac{1}{\epsilon}\tanh\left(\frac{\beta_c\epsilon}{2}\right) - \frac{\tanh\left(\frac{\beta\sqrt{\epsilon^2+\Delta^2}}{2}\right)}{\sqrt{\epsilon^2+\Delta^2}} + \frac{\tanh(\frac{\beta\epsilon}{2})}{\epsilon} - \frac{\tanh(\frac{\beta\epsilon}{2})}{\epsilon}\right] d\epsilon = 0, \tag{1.10}$$

and because

$$\begin{aligned}\int_0^\infty \left[\frac{\tanh(\frac{\beta_c\epsilon}{2})}{\epsilon} - \frac{\tanh(\frac{\beta\epsilon}{2})}{\epsilon}\right] d\epsilon &= \lim_{\epsilon\to\infty}\left[\ln\left(\frac{2\beta_c\epsilon e^C}{\pi}\right) - \ln\left(\frac{2\beta\epsilon e^C}{\pi}\right)\right]_0^\epsilon \\ &= \lim_{\epsilon\to\infty}\left[\ln\left(\frac{T}{T_c}\right)\right] \\ &= \ln\left(\frac{T}{T_c}\right), \end{aligned} \tag{1.11}$$

we can write finally temperature dependence of $\Delta(T)$ in reduced units $\Delta(T)/\Delta(0)$ and T/T_c as

$$\int_0^\infty \left[\frac{\tanh(\epsilon')}{\epsilon'} - \frac{\tanh\left(\sqrt{\epsilon'^2 + \left(\frac{1.764\Delta(T)/\Delta(0)}{2(T/T_c)}\right)^2}\right)}{\sqrt{\epsilon'^2 + \left(\frac{1.764\Delta(T)/\Delta(0)}{2(T/T_c)}\right)^2}}\right] d\epsilon' = -\ln\left(\frac{T}{T_c}\right). \tag{1.12}$$

We see from the above that $\Delta(T)/\Delta(0)$ is a universal function of T/T_c. By calculating the integral numerically, we see that $\Delta(T)/\Delta(0)$ decreases monotonically from $\Delta(T)/\Delta(0) = 1$ at $T = 0$ to $\Delta(T)/\Delta(0) = 0$ at T_c, in the weak coupling assumption of $\hbar\omega_c/k_BT_c >> 1$, as shown in Fig. 1.3.

1.1.2 Electron Tunneling

Classical physics says that, an electron cannot pass through insulator, but basing on the calculation from quantum mechanics, an elementary particle, such as an electron in our case, has a nonzero probability of moving from the conductor on one side of a thin insulating barrier to the other. Insulating layers thicker than a few nanometers are very difficult to penetrate, as the probability of tunneling falls exponentially with thickness. Thus, a very thin layer of insulating layer, normally an oxide layer, is required for electron tunneling, so that the wavefunctions of electrons in the electrodes can overlap. [21] This technique was first presented by Giaever, who has used $Al/Al_2O_3/Pb$ (NIS) junction to confirm the density of states and temperature dependence of energy gap predicted by the BCS theory. [22]

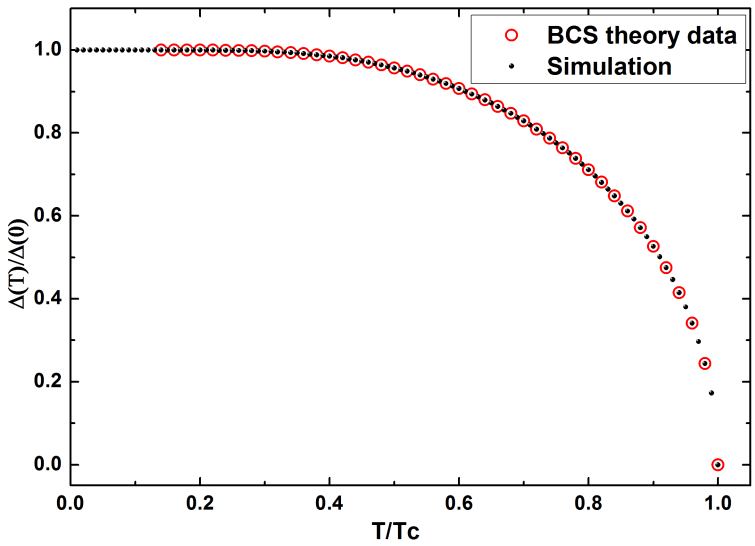

Figure 1.3: Temperature dependence of the energy gap in the BCS theory in weak-coupling limit. The solid line is our computational result, and the square points are gaps data given by *Mühlschlegel* in 1959 from Ref. [20]

The Semiconductor Model and Tunneling Resistance

The electron tunneling through thin insulating layer for different electrodes can be represented in a simple independent-particle (single electron) approximation, as shown in Fig. 1.4,1.5 [21]. In this model, the thin barrier is represented by a trapezoidal shape, normal metal has a continuous Fermi-Dirac distribution of independent particle energy states with density $N(0)$ around Fermi level. The superconductor has the following density of states (DOS) according to BCS theory in the weak-coupling limit: $N(0)V << 1$

$$n_s(E) \equiv \frac{N_s(E)}{N(0)} = \begin{cases} \frac{|E|}{\sqrt{E^2-\Delta^2}} & ,|E| > \Delta \\ 0 & ,|E| < \Delta, \end{cases} \tag{1.13}$$

where there are no states within the gap of width 2Δ created at ϵ_F, as shown in Fig. 1.5

With this model, if there is an available final state, electron can "horizontally" tunnel through the insulating barrier basing on the calculation from quantum mechanics and energy conservation. The net tunneling current I from metal 1 to metal 2 at bias voltage V and temperature T can be commutated simply by summing up all the independent tunneling events of all

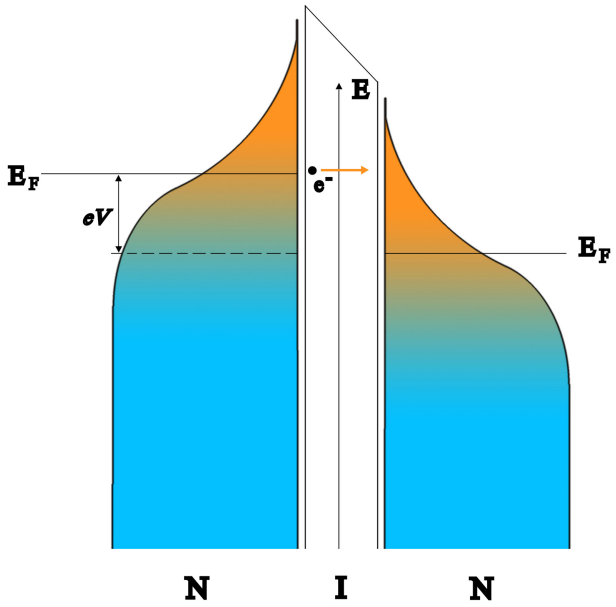

Figure 1.4: The energy diagram for NIN junction with voltage bias eV. Electrons in occupied states will tunnel through insulating barrier into the unoccupied states in the other normal metal.

energies, written as [21, 23]:

$$I = \frac{4\pi e}{\hbar} |T|^2 \int_{-\infty}^{\infty} N_1(E) N_2(E + eV)[f(E,T) - f(E + eV, T)]dE \quad (1.14)$$

where $N(E)$ is the normal or superconducting density of states, and $|T|$ is a tunneling-matrix element determined by the barrier parameters. Here, we assumed that $|T|^2$ is a constant over the energy values of interest, which is a good approximation for small bias voltage $V \approx \Delta$

If both electrodes are normal conductors, as shown in Fig. 1.4, Eq. 1.14 becomes:

$$\begin{aligned} I_{NIN} &= \frac{4\pi e}{\hbar} |T|^2 N_1(0) N_2(0) \int_{-\infty}^{\infty} [f(E,T) - f(E + eV, T)]dE \\ &= \frac{4\pi e}{\hbar} |T|^2 N_1(0) N_2(0) eV \\ &\equiv \frac{1}{R_T} V \end{aligned} \quad (1.15)$$

where $R_T = [4\pi e^2 |T|^2 N_1(0) N_2(0)]^{-1} \hbar$ is a well-defined ohmic tunneling-resistance, independent of V.

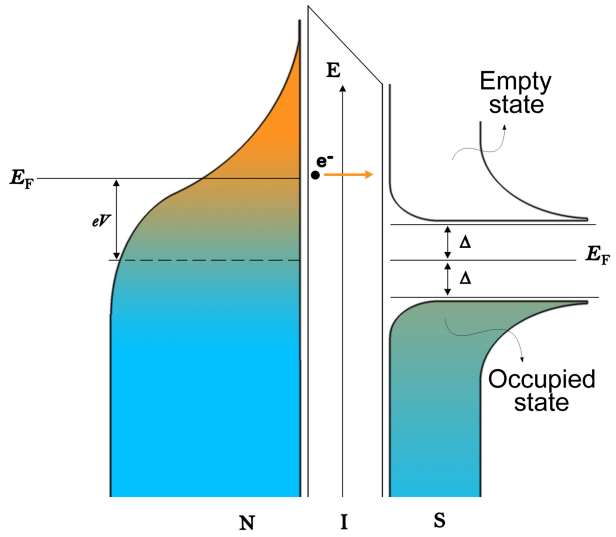

Figure 1.5: The energy diagram for NIS junction with voltage bias eV. Occupied electrons above the BCS gap will tunnel through the insulating barrier into the empty states in the superconductor.

Normal metal-Insulator-Superconductor (NIS) tunneling

The main difference between the NIS junction and NIN junction is one that of the electrodes is a superconductor, which has the quasiparticle density of states $n_s(E)$ as shown in Eq. 1.13. Hence there are ideally no states for electron tunneling within the BCS energy gap $|E| < \Delta$. The energy diagram of the NIS junction and BCS gap are shown in Fig. 1.5, where R_T is the tunneling resistance derived for the NIN junction.

Quantitatively, the tunneling current can be calculated numerically by applying the superconductor DOS, Eq. 1.13, to Eq. 1.14:

$$\begin{aligned} I_{NIS} &= \frac{4\pi e}{\hbar} |T|^2 N_N(0) N_S(0) \int_{-\infty}^{\infty} n_S(E)[f_N(E - eV, T_N) - f_S(E, T_S)]dE \\ &= \frac{1}{eR_T} \int_{-\infty}^{\infty} n_S(E)[f_N(E - eV, T_N) - f_S(E, T_S)]dE \end{aligned} \tag{1.16}$$

The qualitative behavior of the tunneling current is shown in the current-voltage characteristics diagram in Fig. 1.6. At $T \to 0$, for low bias voltage $|eV| < \Delta$, electrons cannot tunnel from the occupied states of normal metal to superconductor, where the corresponding energy levels are either forbidden or occupied, and thus the current through the junction is very small. When

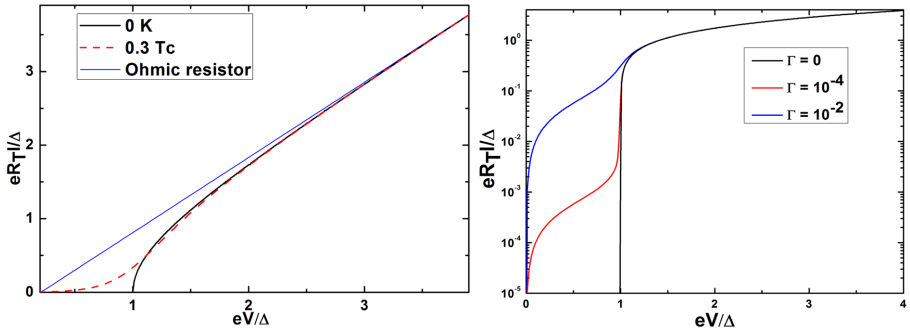

Figure 1.6: Reduced Current-Voltage Characteristic of NIS junction.In (a), the black solid line shows tunneling current at T=0 K with a sharp jump at $eV = \Delta$, and the red dashed line gives an exponential tail at $|eV < \Delta|$ due to the thermal excitation, the blue solid line shows the ohmic behavior of a resistor. (b) shows current broadening in the sub-gap region due to different Γ values at T=0.01Tc.

the bias voltage is higher than the gap, the current will sharply increase at $|eV| = \Delta$ due to the infinite DOS at the edge of the energy gap, and then approaches linear behavior as shown in Fig. 1.6 (a). For $T > 0$, some electrons are thermally excited to higher energies, allowing them to tunnel at a lower voltage, giving an exponential tail to the current in the region below $eV = \Delta$.

Due to finite lifetime effects, in most measurements of NIS junctions, a small linear leakage current in the sub-gap region at low voltage bias is always observed [24,25], which is demonstrated in Fig. 1.6 (b). This leakage current is normally introduced in a phenomenological model as a broadening parameter Γ in the superconductor density of states [26]:

$$n_s(E) = \left| \mathrm{Re} \frac{E + i\Gamma}{\sqrt{(E + i\Gamma)^2 - \Delta^2}} \right| \tag{1.17}$$

Recently, it was shown that in Al it typically results from unintended photo-assisted tunneling by the environment [26].

This broadening parameter Γ can also strongly depend on the quality of the evaporated films [25], and is typically of the order $\Gamma/\Delta \approx 1 \times 10^{-4}$ for evaporated Al films in standard setups [26].

Josephson Tunnel Junction

A Josephson junction, first discussed by Josephson in 1962, is a weak link between two superconducting electrodes, which are normally separated from each other by an insulating barrier, or a short normal metal island [21, 27].

Let's discuss first the quasiparticle current using the superconductor density of states for both electrodes which biased at finite voltages:

$$\begin{aligned} I_{SIS} &= \frac{4\pi e}{\hbar} |T|^2 N_{S1}(0) N_{S2}(0) \int_{-\infty}^{\infty} n_{S1}(E-eV) n_{S2}(E) [f(E-eV) - f(E)] dE \\ &= \frac{1}{eR_T} \int_{-\infty}^{\infty} \frac{|E-eV|}{\sqrt{(E-eV)^2 - \Delta_1^2}} \frac{|E|}{\sqrt{E^2 - \Delta_2^2}} [f(E-eV) - f(E)] dE \end{aligned} \tag{1.18}$$

where Δ_1 and Δ_2 are the BCS energy gaps for the two superconductors.

The I-V characteristic, calculated from Eq. 1.18 and shown in Fig. 1.7, indicates that since the DOS is infinite at the gap edges, there is a discontinuous jump in I_{SIS} around $eV = \Delta_1 + \Delta_2$. At $T > 0$, there is also a second sharp peak at $eV = |\Delta_1 - \Delta_2|$, due to the thermal excitations, the so called singularity matching peak.

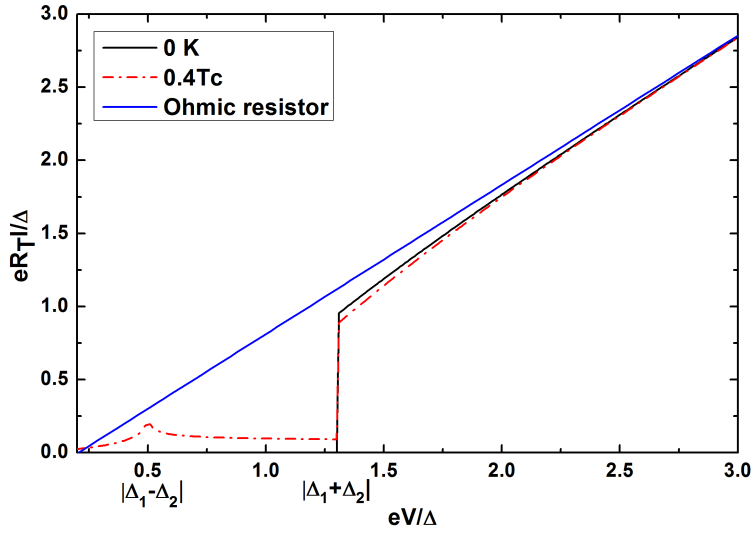

Figure 1.7: Reduced Current-Voltage characteristic of SIS junction with different gap values Δ_1 and Δ_2. Black Solid line is the current response at T=0 K, an it has a discontinuous jump at $\Delta_1 + \Delta_2$. Red dashed line shows a second peak at $|\Delta_1 - \Delta_2|$ when T> 0 K due to the thermal excitation.

There is also a special component which we can discuss by introducing the macroscopic wavefunction $\psi = \sqrt{n_s}e^{i\theta_j}$, to describe superconducting ground state according to the *Ginzburg-Landau* theory [18]. The coupling of the wavefunction between the superconductors will give a finite current at zero-bias voltage, known as *DC Josephson relation*:

$$I_s = I_c \sin\phi, \tag{1.19}$$

where $\phi = \theta_1 - \theta_2$ and I_c is the critical current given by *Ambegaokar-Baratoff relation* for tunnel junctions [28]:

$$I_c = \frac{\pi\Delta}{2eR_T} \tanh\left(\frac{\Delta}{2k_BT}\right). \tag{1.20}$$

Furthermore, there is also an *AC Josephson effect*, which describes the rate of phase change under a finite voltage applied across the junction as

$$\frac{d\phi}{dt} = \frac{2e}{\hbar}V, \tag{1.21}$$

and hence there is also an alternating current:

$$I = I_c \sin(\frac{2eV}{\hbar}t + \phi_0) \tag{1.22}$$

with frequency $\omega = 2eV/\hbar$.

1.2 SINIS Thermometry

A NIS junction, according to Eq. 1.16, has strongly temperature dependent non-linear current-voltage characteristics, which is a very attractive property for low temperature thermometry. This idea was first presented by Rowell and Tsui in 1976 [29] in measuring hot electron temperature in $InAs$, and has since then been used in a wide range of applications in many fields [3,30–34].

In practice, two NIS junctions are used in series with symmetric geometry (SINIS) in order to enhance the signal responsivity. The tunneling current Eq. 1.16 can also be written in a symmetric form for a single junction:

$$I(V,T) = \frac{1}{2eR_T}\int_{-\infty}^{\infty} n_S(E)[f_N(E - \frac{eV}{2}, T_N) - f_N(E + \frac{eV}{2}, T_N)]dE \tag{1.23}$$

We can easily see from this equation that the Fermi-Dirac distribution of the superconductor has been removed, and thus the tunneling current depends only directly on the electron temperature of the normal metal island. The temperature of the superconductor, in practice, can only affect tunneling current through the energy gap $\Delta(T)$ in the superconductor DOS $n_s(E)$, if $T > 0.4T_c$.

In addition, from Eq. 1.23, we can see that the I-V characteristic of a SINIS device at a certain temperature is, in principle, only determined by two parameters: the tunneling resistance R_T and the energy gap $\Delta(T)$, which both can be obtained from the I-V data itself. This feature makes the SINIS thermometer a primary thermometer, in principle. However, non-idealistics such as asymmetry and finite broadening Γ complicate the picture [35], and make it, in practise, usually a secondary thermometer.

SINIS thermometer is normally operated under constant current bias, and the voltage response is measured with a differential voltage amplifier.

According to Eq. 1.23, the I-V characteristic at different bath temperatures are different, thus, at constant current bias, a different temperature of the normal metal will give a different voltage response, as shown in Fig. 1.8(a). Furthermore, the figure also shows that a different current bias value will result in different sensitivity values at different temperature regimes. We can see from the two current bias, $2eR_TI/\Delta = 0.1$ and 0.01 in Fig. 1.8(a), represented as two horizontal dash lines, that the smaller bias (0.01) will give a stronger slope at low temperature range ($T < 400$ mK), but loses sensitivity at high temperature ($T > 400$ mK). At this high temperature range, the higher current bias (0.1) will give larger responsivity, but it is reduced at low temperature as shown in Fig. 1.8(b). Therefore, a working SINIS thermometer always has to be biased properly for optimized sensitivity.

A SINIS double junction device has a number of advantages that make it a promising thermometer for low temperatures. The small structure size makes it easy to integrate into other devices and measure the temperature locally. Self-heating can be kept at a low level by operating in the sub-gap region, where the current is very small. Sensitivity can be easily optimized by changing the bias as discussed above. However, there are also drawbacks for this technique. For example, due to the finite life-time broadening of DOS in Eq. 1.17, the leakage current will affect the I-V curves, and result in a deviation from measured voltage shown in Fig. 1.9(a) and thus the corresponding $V - T$ curves shown in Fig. 1.9(b).

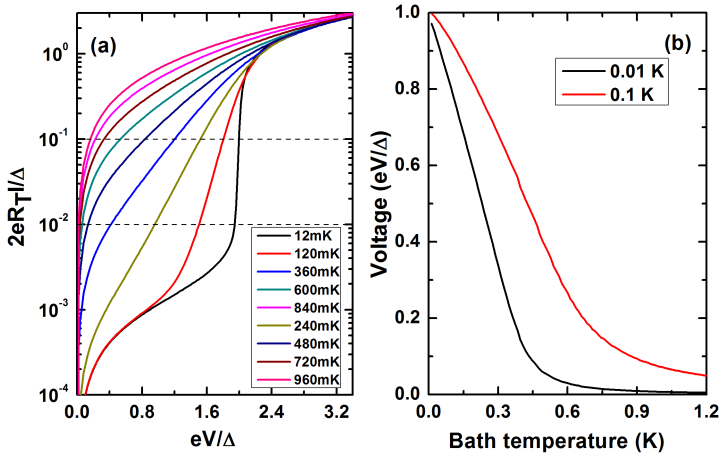

Figure 1.8: (a) Calculated current-voltage characteristics of a SINIS thermometer at different temperatures based on Eq. 1.23. Dash horizontal lines represent two different current bias 0.1 and 0.01 in reduced units. (b) Temperature-voltage behavior of SINIS thermometer at current bias shown in (a).

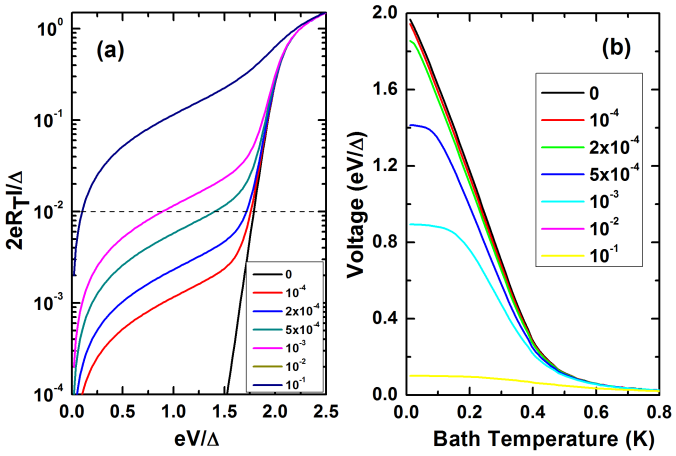

Figure 1.9: (a) A calculation of current-voltage characteristics of a SINIS thermometer with different DOS broadening parameters Γ, shown in legend. (b) Voltage-temperature behavior of SINIS thermometer at current bias shown with a dashed line in (a).

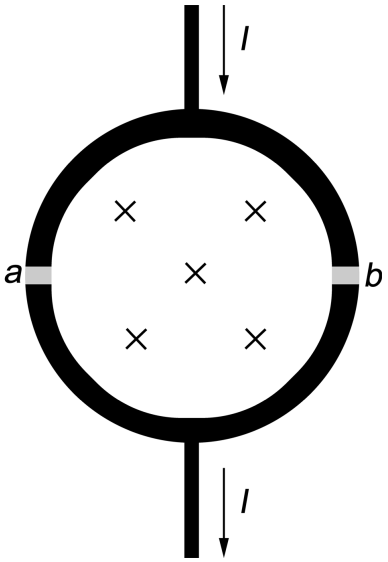

Figure 1.10: A schematic of a SQUID loop. The black line represents an superconductor line, and the grey area a and b are insulators.

1.3 SQUID

The SQUID is an acronym for Superconducting Quantum Interference Device. It is an extremely sensitive device for measuring a small magnetic field by using a superconducting loop with two Josephson junctions.

The basic configuration for a DC SQUID loop is shown in Fig. 1.10. A superconducting loop with two Josephson junctions is placed in the middle of a superconducting line, and divides the supercurrent into two branches. Along each path, the separated supercurrent has its own phase difference δ_a and δ_b due to the junction in their path. A magnetic field through the loop causes further shifts in this phase, which will have a periodic dependence on the applied magnetic field.

The supercurrents that goes through the junction a and b are:

$$I_{a,b} = Aj_0 \sin \delta_{a,b} \tag{1.24}$$

where A is the junction area, j_0 is the current density in the superconducting loop, and, if assuming the junctions are identical, the phase shift of each junction can be written as

$$\delta_a = \delta_0 + \frac{e}{\hbar}\Phi \tag{1.25}$$

$$\delta_b = \delta_0 - \frac{e}{\hbar}\Phi \tag{1.26}$$

where e is the electron charge, $\hbar$ is Plancks constant divided by 2π and Φ is the magnetic flux through the loop. Then the supercurrent can be written as

$$I = 2Aj_0 \cos\left(\frac{e\Phi}{\hbar}\right) \sin\delta_0 \tag{1.27}$$

A SQUID can be used as an extremely sensitive magnetometer, with a minimal measurable field as low as 5×10^{-18}T [36]. It can also be a very sensitive ammeter by introducing the current signal into a superconducting input inductor to generate an electromagnetic flux through the SQUID. [37, 38]

1.4 Inductance and Electromagnetic Coupling

1.4.1 Inductance Calculation

Inductance is the ability of an inductor to store energy in a magnetic field, it is the key parameter in linking sample electronics to the magnetic field coupling.

The self inductance L, which parametrizes magnitude of the opposing voltage generated by the rate of change in current in the inductor, is quantitatively defined by the well-known Faraday's law

$$v = N\frac{d\Phi}{dt} = L\frac{di}{dt} \tag{1.28}$$

where v is the voltage generated in the inductor, N is the number of turns of the inductor, Φ is the total magnetic flux through the loop, and i represents the current in the inductor circuit.

The mutual inductance M, which describes the voltage induced in one electrical circuit by the rate of change of the electric current in another nearby inductor, is also a very important measure of the coupling between two inductors, and it is normally expressed with a dimensionless coupling coefficient k in the relationship with self inductances:

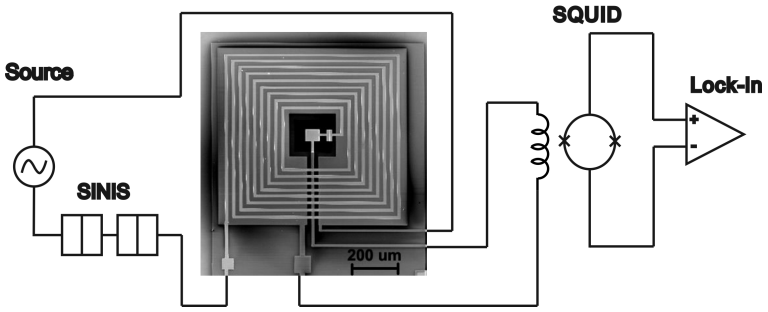

Figure 1.11: A Scanning electron microscope image of one pair of the sample washer and input coil structure. The SEM image is integrated into a simplified schematic of our measurement setup. The input coil is connected to the tunnel junction and the washer is connected to the SQUID input coil.

$$M = k\sqrt{L_1 L_2}. \tag{1.29}$$

In our sample structure design, shown in Fig. 1.11, the output circuit is a planar washer type inductor, which is used for coupling the magnetic field from the input coil and transports the current to the SQUID input through a superconducting circuit. The inductance of the washer can be calculated from the model of square washer with hole as [39]:

$$L_w = L_h = 1.25\mu_0 d \approx 0.314\text{nH} \tag{1.30}$$

where d=200μm is the diameter of the washer hole and μ_0 is the vacuum permeability.

The input circuit, which directly connects to the SINIS junction and is used for generating the magnetic field from the sample current signal, is a concentric square coil. The inductance of the input coil can be calculated as [40]

$$L_i = N_i^2(L_h + L_{sl}/3) + lL_{strip} \tag{1.31}$$

where N_i=9 is the number of turns of the input coil, L_{sl} ≈3 pH is the slit inductance for a 10 μm slit [40], l=16.4 mm is the total length of the input coil, and L_{strip} is the stripline inductance [41]:

$$L_{strip} \approx \mu_0 \frac{h + \lambda_{L,w} + \lambda_{L,i}}{w_i + 2(h + \lambda_{L,w} + \lambda_{L,i})} \tag{1.32}$$

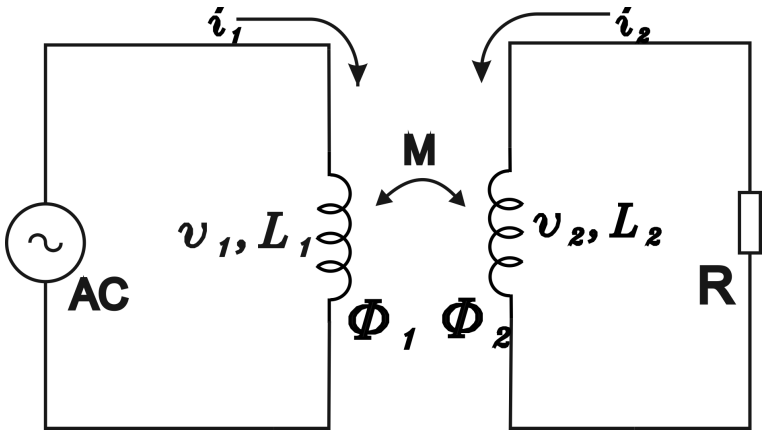

Figure 1.12: A schematic shows the magnetic coupling between two inductors.

where h=400 nm is the thickness of the AlO_x dielectric layer between the washer and input coil, $\lambda_{L,w}$ = 315 nm and $\lambda_{L,i}$ = 210 nm are London penetration depths of washer and input coil respectively [42], and w_i=10 μm is the linewidth of the input coil, and thus L_{strip} ≈625 nH/m.

Therefore, we can calculate the expected inductance of the input coil as:

$$L_i = 9^2(0.314 + 3 \times 10^{-3}/3) + 16.4 \times 10^{-3} \times 625 = 35.7nH \tag{1.33}$$

1.4.2 Electromagnetic coupling for superconductor

The electromagnetic coupling in a superconducting circuit is slightly different from the Faraday's law that applies for the normal metal. In the coupling of the two inductors shown in Fig. 1.12, the magnetic flux in L_2 is $\Phi_2 = Mi_1 + L_2 i_2$. According to Faraday's law we have

$$v_2 = \frac{d}{dt}\Phi_2 = \frac{d}{dt}(Mi_1 + L_2 i_2) = -i_2 R, \tag{1.34}$$

R will disappear when the circuit goes into superconducting state leaving

$\Phi_2 = Mi_1 + L_2 i_2 = Const.$, if there is no flux initially in the second winding, $\Phi_2 = 0$, then

$$Mi_1 = -L_2 i_2, \tag{1.35}$$

this gives the current gain $\beta_I \equiv i_2/i_1 = M/L_2$.

Additionally, due to the Meissner effect, we can also have a magnetic flux density transformer from the magnetic coupling. A schematic of su-

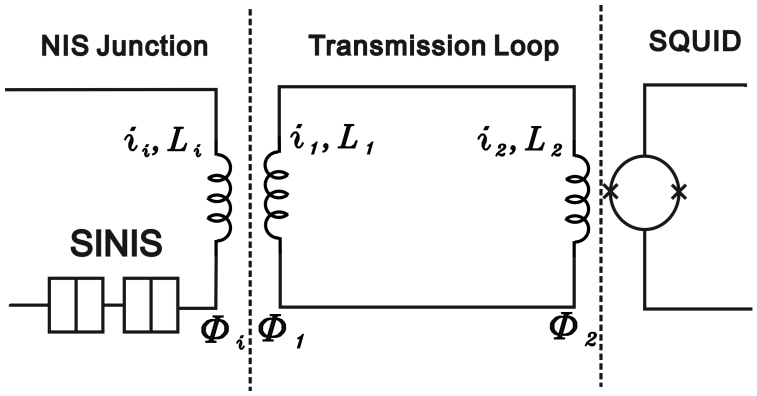

Figure 1.13: A lumped circuit shows the magnetic coupling in the transmission line in the sample structure. Current signal coming from SINIS junction will magnetically coupled into the transmission loop which is kept superconducting, and then coupled to a SQUID.

perconducting transmission circuit is shown in Fig. 1.13, where we have an input current i_i, input inductance L_i, transmission loop current i_t, loop input inductance L_1, SQUID input inductance L_2, and a SQUID read out. The magnetic flux in the transmission input inductor is $\Phi_1 = M_i i_i + L_1 i_t$, and in the SQUID input inductor is $\Phi_2 = L_2 i_t$. Base on the Meissner effect, with no trapped flux in the transmission loop, we have

$$\Phi_1 + \Phi_2 = M_i i_i + L_1 i_t + L_2 i_t = 0 \tag{1.36}$$

therefore we find:

$$L_2 i_t = M_i i_i \frac{L_2}{L_1 + L_2} \tag{1.37}$$

If we measure the magnetic flux density $B_2 = \Phi_2 / N_2 A_2$ for this transmission loop, we get field gain β_B which can be calculated:

$$\beta_B \equiv \frac{B_2}{B_i} \approx \frac{N_1 A_1}{N_2 A_2} \frac{M L_2}{L_i (L_1 + L_2)} \tag{1.38}$$

where N is the number of turn and A is the area of the coil.

This method can be used to increase the amplification of the magnetic flux density by carefully designing and optimizing the sample circuit structure.

1.5 ^{3}He-^{4}He Plastic Dilution Refrigerator

This section describes the operating principles of the ^{3}He-^{4}He Plastic Dilution Refrigerator used in this work.

1.5.1 Properties of the Helium Isotopes

After Dutch physicist H.Kamerlingh Onnes had successfully liquified helium at the temperature of 4.2 K in 1908 [43], liquid helium became the most important substance for low-temperature experiments. In order to reach a temperature below about 10 K, almost all refrigeration processes need to use liquid helium exclusively, or as a pre-cooling method. Therefore the liquification opened a new era in low-temperature physics, and had a significant impact on solid state physics research.

^{4}He is the common stable helium isotope, whose nucleus contains two protons and two neutrons, each with anti-parallel nuclear spin orientation. Therefore, ^{4}He is a Bose particle with total nuclear spin $I = 0$. Today, ^{4}He is obtained exclusively from helium-rich natural-gas sources, and normally costs 7 to 10 euro per liter of liquid [44].

The rare stable helium isotope, ^{3}He has a nucleus containing two protons but only one neutron, which gives a total nuclear spin $I = 1/2$, and makes ^{3}He a Fermi particle. ^{3}He exists in the natural gaseous sources with ^{3}He/^{4}He abundance ratios around 0.5 to 3×10^{-7}. It is also contained in atmosphere with a abundance ratio 1.2×10^{-6} [45]. But nowadays, ^{3}He is commonly produced from tritium by diffusion processes in nuclear reactor, which can provide necessary quantities for industrial use but with a high price about 100 euro per liter of gas [46]. Current price is even higher.

Some important properties and phase diagrams of the two stable helium isotopes are shown in Table 1.5.1 and Fig. 1.14 [46]. As shown in Table 1.5.1, ^{3}He and ^{4}He have very low boiling points and critical temperatures, and they do not have a solid phase at their own vapor pressure even at 0 K. They have identical van der Waals forces and identical chemical behavior, since they share the same electronic structure. However, because of the difference between the nuclear structures, there are also distinct differences in their physical properties at low temperatures. First, the different total nuclear spin results in different statistics: boson is for ^{4}He and fermion is for ^{3}He. Second, the mass difference between the nuclei leads to different

Table 1.1: Properties of liquid helium [46]

Properties	^{3}He	^{4}He
Boiling point, $T_b(K)$	3.19	4.21
Critical temperature, $T_c(K)$	3.32	5.20
Superfluid transition temperature, $T_s(K)$	0.0025	2.1768
Density[a], $\rho(g\ cm^{-3})$	0.082	0.1451
Classical molar volume[a], $V_m(cm^3\ mol^{-1})$	12	12
Actual molar volume[a], $V_m(cm^3\ mol^{-1})$	36.84	27.58
Melting pressure[b], $P_m(bar)$	34.39	25.36
Minimum melting pressure, $P_m(bar)$	29.31	25.32
Gas-to-liquid volume ratio[c]	662	866

[a] At saturated vapor pressure and $T = 0$ K.
[b] At $T = 0$ K.
[c] Liquid at $1K$, NTP gas(300 K, 1bar).

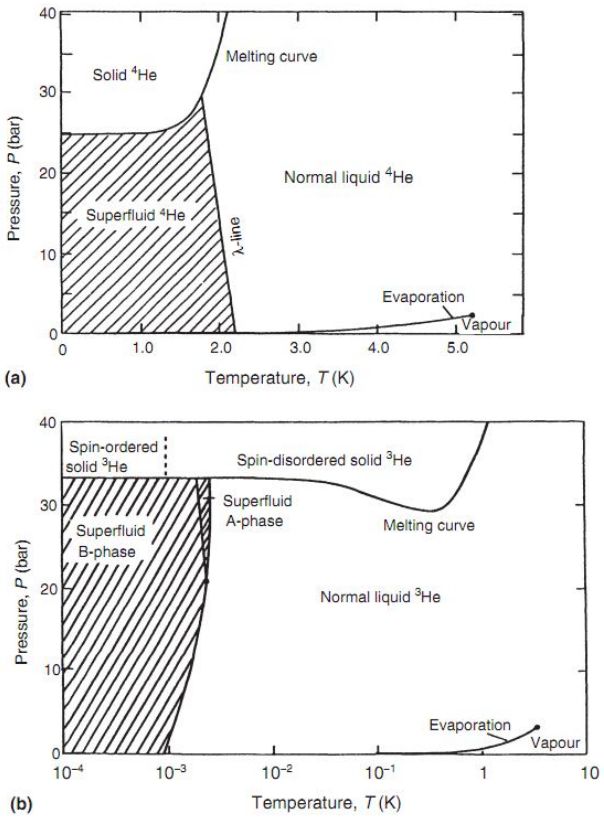

Figure 1.14: Phase diagrams of (a) ^{4}He and (b) ^{3}He. The image takes from Ref. [46]

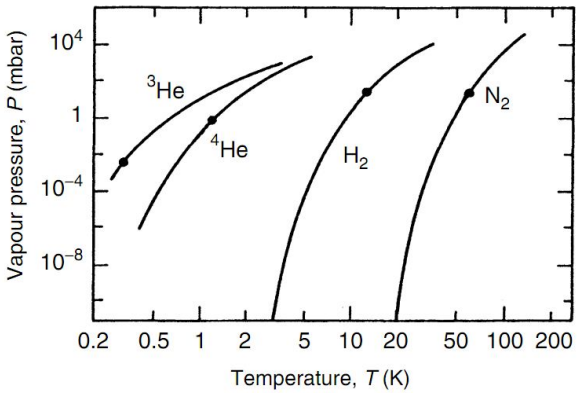

Figure 1.15: The vapor pressure of different cryoliquids. The black dots are the lower temperature limits of vapor pressure refrigerator for corresponding liquid.

quantum mechanical zero-point energy values, which affect many physical properties such as the latent heat of evaporation, vapor pressure and heat capacity.

The larger the zero-point energy is, the smaller the latent heat of evaporation, and the higher the vapor pressure will be. The zero point energy E_0 depends on nucleus as:

$$E_0 = \frac{h^2}{8ma^2}, \tag{1.39}$$

so that helium, which has a small atomic mass m, has a large zero-point energy compared to other cryoliquids. Thus it has a smaller latent heat of evaporation and a larger vapor pressure.

The vapor pressure can be calculated from the Clausius-Clayperon equation

$$\left[\frac{dP}{dT}\right]_{vap} = \frac{S_{gas} - S_{liq}}{V_{m,gas} - V_{m,liq}} \tag{1.40}$$

where S is entropy and V_m is molar volume.

If we assume that the latent heat of evaporation in low temperature range is roughly constant, then the temperature dependent vapor pressure is

$$P_{vap} \propto e^{-L/RT} \tag{1.41}$$

The temperature dependence of vapor pressure for different cryoliquids is shown in Fig. 1.15. Helium isotopes have substantially higher vapor pressure

than other liquids at low temperature, especially in the regime below 2 K. This high vapor pressure gives helium many advantages as a cryogenic liquid for low temperature cryostats. First, in the temperature regime around 1 K, the gases other than helium have an extremely low vapor pressure, and will condensate onto the cold surfaces of the refrigerator. This "cryo-pump" is so efficient that it can be used to improve the vacuum for a low-temperature apparatus. Secondly, by pumping out helium vapor, one can lower the liquid temperature further below the boiling point at normal pressure. This can be used as a refrigerator in many low temperature experiments, and it is also a very important component for our ^{3}He-^{4}He dilution refrigerator used in this thesis. In practice, since the pumps commonly used work as a constant-volume pumps with speed $\dot{V}$, the cooling power of this vapor pressure refrigerator is given by [46]

$$\dot{Q} = \dot{n}(H_{liq} - H_{gas}) = \frac{\dot{V}LP_{vap}}{RT} \tag{1.42}$$

where P_{vap} is proportional to $e^{-1/T}$ as shown in Eq. 1.41.

Thus the cooling power $\dot{Q} \propto e^{-1/T}$, and a refrigerator that relies on pumping in practice has a low temperature limit 1.3 K for ^{4}He and 0.3 K for ^{3}He.

1.5.2 Properties of ^{3}He-^{4}He Mixtures at Low Temperatures

In 1962, a novel method for continuous refrigeration with liquid helium for temperatures lower than 0.3 K was proposed by H. London, G.R. Clarke, and E. Mendoza [47]. Different from the vapor pressure refrigerator, this new technique is based on using the heat of mixing of the two helium isotopes to obtain a low temperature rather than the latent heat of evaporation. Today, a ^{3}He-^{4}He dilution refrigerator can easily reach 50 mK, and even if by one home-made refrigerator in a compact scale (e.g. the refrigerator used in this thesis). Slightly below 2 mK can be reached by more complicated commercial refrigerator [48]. It has become the most widely used refrigeration technology for temperature below 1 K.

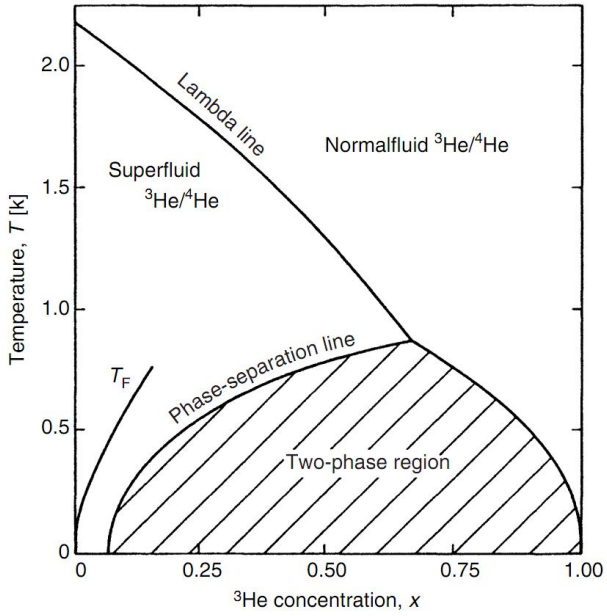

Figure 1.16: Phase diagram of liquid ^{3}He-^{4}He mixtures at saturated vapor pressure. The figure shows the superfluid phase transition λ-line, the phase separation line and the line of the Fermi temperature T_F of the ^{3}He component.

Phase Diagram and Solubility

The concentration-temperature phase diagram of liquid ^{3}He-^{4}He mixture at saturated vapor pressure, shown in Fig. 1.16 [49], is the key to understanding this refrigeration technique.

From the figure, we can see that the temperature of superfluid phase transition line of the mixture (λ-line) is decreased with increasing ^{3}He concentration, and it eventually ceases to exist if the ^{3}He concentration reaches 67.5%. The interesting phenomenon is that, at this point, the λ-line meets the phase separation line: below this temperature the two helium isotopes begin to separate into two phases, each with a certain limiting concentration depending on the temperature, and the shadowed area in the figure becomes a forbidden zone. One phase is rich in ^{4}He and the other is rich in ^{3}He. Because of its lower density, the ^{3}He-rich liquid floats on top of the ^{4}He-rich liquid. If we cool down the mixture further close to absolute zero, the ^{3}He-rich liquid becomes pure ^{3}He. However, the ^{4}He-rich liquid, surprisingly, only reaches a constant ^{3}He concentration of 6.6% rather than being pure ^{4}He. This finite solubility is the most important key to the ^{3}He-^{4}He dilution refrigeration technology, as cooling is achieved by transferring ^{3}He atoms from

the pure ^{3}He phase to the diluted ^{4}He-rich phase. The cooling capacity in this cooling process is the heat of mixing of the two isotopes.

Cooling Power of the Dilution Refrigerator

Similar to the Equation 1.42 of vapor pressure refrigerator mentioned above, the cooling power of the ^{3}He-^{4}He dilution refrigerator can be calculated by replacing the enthalpy of evaporation with the heat of mixing,

$$\dot{Q} = \dot{n}_3[H_d(T) - H_c(T)] \tag{1.43}$$

where $\dot{n}_3$ is the molar flow rate of ^{3}He atoms, and $H_d(T)$ and $H_c(T)$ are the enthalpies of liquid ^{3}He in diluted and concentrated phase, respectively.

Because enthalpy is given by

$$H(T) - H(0) = \int_0^T C(T)dT, \tag{1.44}$$

we can obtain the enthalpy of liquid ^{3}He by using experimental data given by Greywall in 1986 [50], who accurately measured the specific heat of ^{3}He at temperatures below 40 mK and at saturated vapor pressure,

$$C_3 = 2.7RT = 22T \text{ [J/molK]}. \tag{1.45}$$

This gives us the enthalpy of concentrated phase as

$$H_3(T) = H_3(0) + 11T^2 \text{ [J/mol]}. \tag{1.46}$$

To calculate the enthalpy of diluted phase, we can also begin with the specific heat of diluted ^{3}He liquid by using effective mass m^* instead of ^{3}He mass m_3:

$$C_{3,d} = N_0 k_B \frac{\pi^2}{2}\frac{T}{T_F} = 0.745\frac{m^*}{m_3}\left(\frac{V_m}{x}\right)^{2/3} T, \tag{1.47}$$

where

$$T_F = \frac{\hbar^2}{2m^* k_B}\left(\frac{3\pi^2 N_0 x}{V_m}\right)^{2/3} = 55.2\frac{m_3}{m^*}\left(\frac{x}{V_m}\right)^{2/3} \text{[K]} \tag{1.48}$$

is the Fermi temperature for concentration x, and the molar volume of the mixture V_m is

$$V_m = V_{m,4}(1 + 0.284x) \tag{1.49}$$

where the molar volume of pure ^{4}He is $V_{m,4} = 27.589$ cm^3/mol [51].

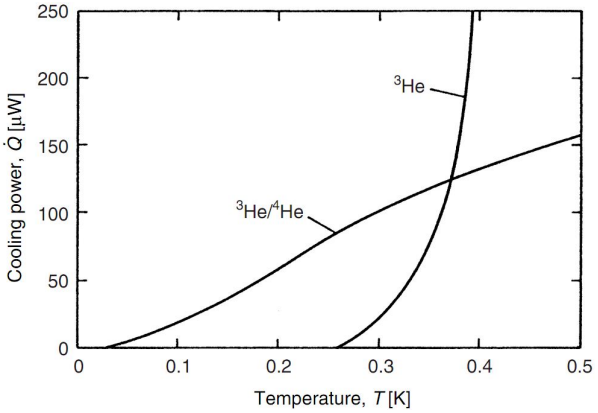

Figure 1.17: The temperature dependence of the cooling power of a ^{3}He evaporation cryostat and of a ^{3}He-^{4}He dilution refrigerator.

For a mixture of $x = 6.6\%$ at saturated vapor pressure, the effective mass is $m^* \approx 2.5m_3$, and thus the specific heat of 6.6% diluted ^{3}He below 40mK is

$$C_{3,d}(6.6\%) \approx 106T \text{ [J/molK]}. \tag{1.50}$$

When the two phases are in thermodynamic equilibrium, we have

$$H_3 - TS_3 = H_{3,d} - TS_{3,d} \tag{1.51}$$

This then gives with Eqs. 1.45, 1.46, 1.50

$$\begin{aligned} H_{3,d}(T) &= H_3(0) + 11T^2 + T\int_0^T \left(\frac{C_{3,d}}{T'} - \frac{C_3}{T'}\right) dT' \\ &= H_3(0) + 95T^2 \text{ [J/mol]} \end{aligned} \tag{1.52}$$

and thus the cooling power of the ^{3}He-^{4}He dilution refrigerator is

$$\dot{Q}(T) = \dot{n_3}[H_{3,d}(T) - H_3(T)] = 84\dot{n_3}T^2 \text{ [W]}. \tag{1.53}$$

Figure 1.17 shows the comparison of the cooling power between ^{3}He evaporation cryostat and the ^{3}He-^{4}He dilution refrigerator at low temperatures. Since the dilution process has cooling power $\dot{Q} \propto T^2$ while the evaporation process is $\dot{Q} \propto e^{-1/T}$ as mentioned above, the cooling power of ^{3}He-^{4}He dilution refrigerator has a much weaker temperature dependence, which gives it a great advantage at temperatures below 0.3K.

Osmotic Pressure

Another key property of ^{3}He-^{4}He mixture is the osmotic pressure. Since the cooling power of the ^{3}He-^{4}He dilution refrigerator is generated from the heat of mixing the two helium isotopes, and if the cryostat needs to work continuously, we have to find a way to circulate the two liquids between separating and mixing.

A still chamber, connected to the mixing chamber, is normally used in a ^{3}He-^{4}He dilution refrigerator, which performs as a ^{3}He evaporation refrigerator as shown in Fig. 1.18. ^{3}He is pumped out of this chamber during the circulation, which forms an osmotic pressure of ^{3}He between the two chambers according to van't Hoff's law [46]

$$\pi_{mc} - \pi_{st} \approx \frac{(x_{mc}T_{mc} - x_{st}T_{st})R}{V_{m,4}} \tag{1.54}$$

where π is the osmotic pressure, mc stands for mixing chamber and st stands for still, $V_{m,4}$ is the molar volume of ^{4}He.

If we assume the concentration of ^{3}He in the still is much smaller than in the mixing chamber, $x_{mc} = 6.6\%$ and $T_{mc} \leq 0.1K$ then

$$\Delta\pi_{max} = \frac{x_{mc}T_{mc}R}{V_{m,4}} \approx 20 \text{ mbar} \tag{1.55}$$

which corresponds to vertically lifting ^{3}He for 1 m from the mixing chamber into still. Thus we can continuously drive the ^{3}He leaving the mixing chamber from bottom, and suck it from the concentrated phase into the dilute phase from top. This osmotic pressure of the ^{3}He-^{4}He mixture makes the idea of a continuous refrigerator feasible, and it is important for the realization of a ^{3}He-^{4}He dilution refrigerator.

1.5.3 Construction of Plastic Dilution Refrigerator

In this work we have built a plastic dilution refrigerator (PDR) based on the design described in Ref. [52].

Basic Design of ^{3}He-^{4}He Dilution Refrigerator

The main principle for a ^{3}He-^{4}He dilution refrigerator was described above. However, in practice, it is much more complicated to build a working refrig-

erator, which will involve multiple cooling and heat exchange steps and more careful designs.

Figure 1.18 shows a typical design of a ^{3}He-^{4}He dilution refrigerator. The ^{3}He gas, which is the key material for cooling process, coming from the room temperature tank, will first be precooled by the liquid ^{4}He bath to 4.2 K. Then it will be condensed into liquid form through a condenser thermally anchored to a 1.5 K ^{4}He evaporation refrigerator, which we call a ^{4}He pot. The liquid ^{3}He will then be further cooled to 0.7 K by the heat exchanger connected to the still, which, as mentioned before, is basically a ^{3}He evaporation refrigerator. After leaving the still, ^{3}He will flow through a series of heat exchangers to cool it to a low enough temperature before it enters the upper, concentrated phase in the mixing chamber.

In the still, at 0.7 K, most of ^{4}He will stay in liquid form, but ^{3}He will evaporate and form a typically 90% concentration ^{3}He vapor above the liquid because ^{3}He has higher vapor pressure at that temperature. Only less than 1% concentration in the liquid in still is ^{3}He. There is a wider tube connecting the bottom of the mixing chamber to the still. The osmotic pressure shown in Eq. 1.55 will drive ^{3}He from the dilute phase in mixing chamber into the still, and then, the ^{3}He in the concentrated phase in the upper parts of the mixing chamber will compensate this loss, and will go across the phase boundary into the diluted phase. At this moment, if we continuously pump the ^{3}He vapor from the still and resupply it to the condensation process above, we will have a closed ^{3}He circulation process, and therefore the ^{3}He-^{4}He dilution refrigerator will operate continuously.

^{4}He Pot

In a ^{3}He-^{4}He dilution refrigerator, the pre-cooling temperature range between $1.3K \leq T \leq 4.2K$ is normally done by a ^{4}He Pot, which basically is a ^{4}He evaporation refrigerator.

In this pot, liquid ^{4}He is drawn from the ^{4}He bath through a flow impedance to a small chamber of several cm^3 inside the main vacuum can in the cryostat. The ^{4}He vapor is then pumped continuously, and the temperature of the liquid decreases as shown in Fig. 1.15 to 1.3 K at lowest.

In the circulation state, the cooling power produced by ^{4}He Pot is mainly used to condense and pre-cool the incoming ^{3}He gas. And, it is also a very important pre-cooling stage for all the wires and connections that go below

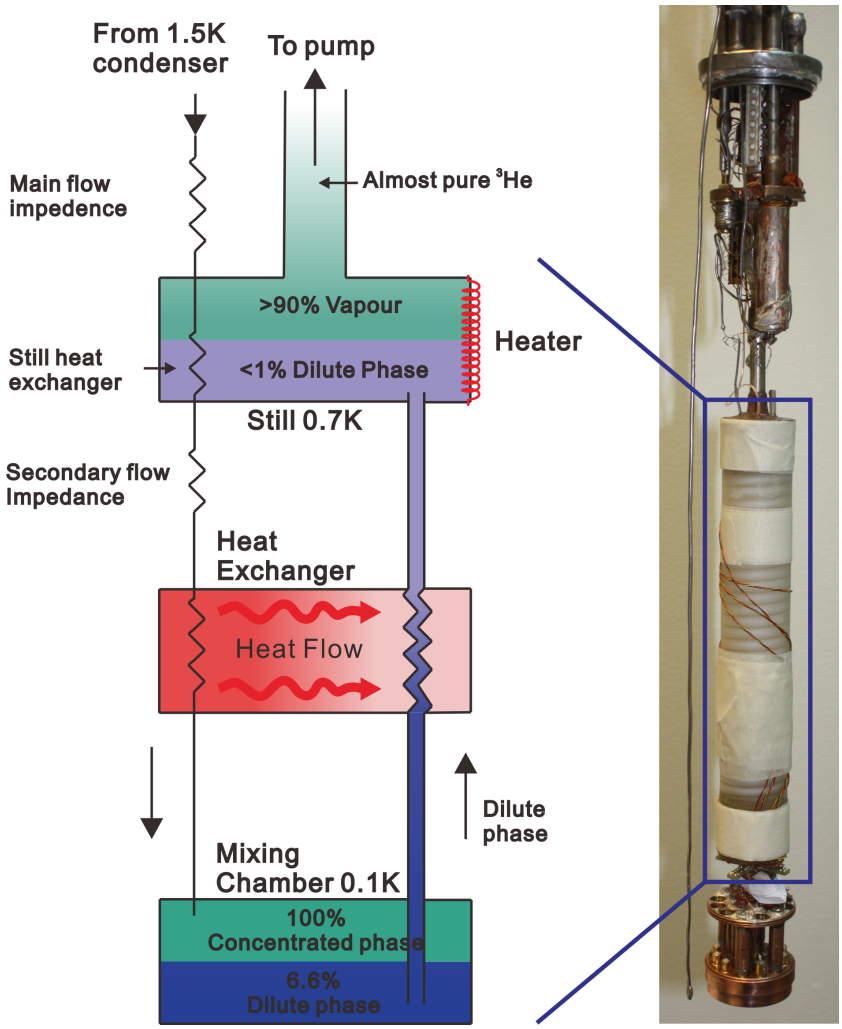

Figure 1.18: Schematic (left) of a basic design of still and mixing chamber of the ^{3}He-^{4}He dilution refrigerator we used in this thesis. The picture on the right shows the real structures which are enclosed in a vacuum jacket that is immersed in the 4.2K ^{4}He bath during experiment. The structures shown in the schematic are built inside the plastic chamber as shown in the picture.

this stage.

Still

The still, as we discussed above, is a key part of a ^{3}He-^{4}He dilution refrigerator. It is first of all the place where the ^{3}He vapor is pumped to produce enough osmotic pressure to the mixing chamber for the ^{3}He circulation. Also, it will cool the liquid ^{3}He coming from the 1.3 K condenser down to 0.7 K through a heat exchanger thermally anchored to the still. Also, any connections and electrical leads should be heat sunk to the still as well, especially for our PDR.

If we assume the liquid ^{3}He is cooled from 1.3 K to 0.7 K at still, according to the enthalpy balance

$$\dot{n}_3 L_3(T_{st}, x_{d,st}) = \dot{n}_3[H_3(T_{cond}) - H_3(T_{st})] + \dot{Q}_{st} \tag{1.56}$$

there is a heat rate requirement for $\dot{Q}_{st}$ [W]$\approx 40\dot{n}_3$ [mol]. This can be done by mounting a still heater in the chamber, which normally is set to about few milliwatts to supply the heating power to still.

Heat Exchanger

Heat exchangers are arguably the most important and critical parts of a dilution refrigerator. The purpose of the heat exchangers is to bring the temperature of the incoming ^{3}He as close to the temperature of the mixing chamber as possible, by using the cold mixture leaving the mixing chamber to pre-cool the incoming ^{3}He, and thus act as a final step to reduce the heat load from room temperature. A powerful heat exchanger is expected to have a good conductivity between the liquids, have no vertical heat conductivity, have a small volume so that the liquids can quickly reach equilibrium, and have a small impedance so that the viscous heating due to flow is small. Normally, especially in commercial dilution refrigerators, a series of heat exchanger steps are used to achieve optimal cooling.

However, in our ^{3}He-^{4}He dilution refrigerator, we use a rather simple heat exchanger design to reach a minimum temperature slightly higher than commercial ones. Shown schematically in Fig. 1.19, we use a continuous counterflow tube-in-tube heat exchanger consisting of two concentric capillaries. The one with smaller diameter contains the incoming warmer ^{3}He, and is coiled into a spiral in order to increase the surface area. The outer one

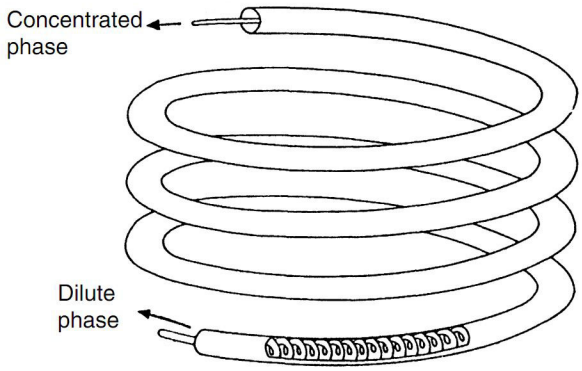

Figure 1.19: Schematic of a concentric heat exchanger. The concentrated phase ^{3}He moves in the inner coil into the upper part of mixing chamber, and the outer capillarie contains the dilute phase of ^{3}He from the bottom of mixing chamber to still.

contains the diluted ^{3}He coming from mixing chamber to the still. In such a heat exchanger the heat is transferred across the inner wall of the capillary and the temperature changes continuously along the exchanger.

Mixing Chamber

The optimal cooling power of the mixing chamber was already shown in Eq. 1.53. Generality to the case where the incoming concentrated phase has a higher temperature we have,

$$\dot{Q}(T) = \dot{n_3}[H_{3,d}(T_{mc}) - H_3(T_{ex})] = \dot{n_3}[95T_{mc}^2 - 11T_{ex}^2] \text{ [W]}, \tag{1.57}$$

where T_{mc} is the temperature of the ^{3}He dilute phase in the mixing chamber, and T_{ex} is the temperature of the incoming ^{3}He concentrated phase. If the concentrated ^{3}He leaving the last heat exchanger has a temperature equal to the temperature of the mixing chamber or we operate the cryostat in a discontinuous mode (which means there is no warm concentrated ^{3}He resupplied to mixing chamber), Eq. 1.57 reproduces the earlier maximum cooling power result

$$\dot{Q}_{max} = 84\dot{n}_3 T_{mc}^2 \tag{1.58}$$

This cooling power is used to compensate the extra heat load from wiring and other power loads and is used to cool down the experiment setup through a sintered silver powder heat exchanger with surface areas several m^2.

However, if the heat exchanger is not designed properly, the incoming concentrated ^{3}He will have much higher temperature. According to Eq. 1.57, if $T_{ex} \geq 3T_{mc}$, the cooling power $\dot{Q}$ will go to zero, and will become heating instead. This fact again emphasis the importance of the heat exchanger of the ^{3}He-^{4}He dilution refrigerator.

Chapter 2

Fabrication

2.1 Equipment

2.1.1 Electron Beam Lithography

Electron beam lithography (EBL) is a standard tool in modern nanofabrication processes. It is uses a focused beam of electrons to scan a patterned area, which has been covered with a polymeric or an other electron sensitive material (called resist). [53]

EBL machine generally consists of three main parts: the electron source, the magnetic lens system, and the beam control and detection system. Electrons are generated from either a thermionic source, where electrons are emitted from a heated conducting cathode material, like in the LEO 1430 system we have used, or generated by a field emission source, in which an electric field is used to give electrons sufficient energy to be emitted, like in the Raith e-LiNE system used in this thesis. After generation, the e-beam is focused into a point of diameter $\sim$ 10 nm through a series of computer controlled electromagnetic lenses and finally onto the substrate surface.

The exposing of the resist by the electron beam will selectively "remove" it, either from the exposed or the non-exposed regions, depending on the type of resist used. In a positive resist, due to the main polymer chain scission, the exposed areas become soluble to certain developer chemicals, such as the mixture of methyl isobutyl ketone (MIBK) and isopropanol (IPA), as was used in this thesis. For the negative resist, the exposure will induce cross linking in the resist materials, and thus the exposed resist will be left after the treatment with a developer. The purpose of the EBL is to directly

transfer a pattern from a design program to the substrate material, the same way as with photolithography [53]. Because it is not limited by the diffraction of light, EBL can create much higher resolution patterns compared to traditional photolithography. Nowadays, the resolution of EBL generally can reach down to ~ 5 nm, which is limited primarily by the forward-scattering of electrons within the resist material and from the substrate surface.In this thesis, most of the work and the final sample is fabricated by the Raith e-LiNE system, whose specifications can be found in Appendix A.

2.1.2 Physical vapor Deposition

Physical vapor deposition (PVD) is the dominant method for metallic thin-film deposition. The basic idea of PVD is to eject the material from a solid target material, and transport it ballistically to the substrate surface in a high vacuum chamber. In thermal evaporation, the source material is normally heated either by Joule heating, where a DC current source is used to directly heat the crucible containing the metal, or by a focused electron beam, that creates a local hot spot in the source. In our evaporators, the e-beams are generated from a filament and steered and focused into the crucible by a magnetic field and rastering. The ejected materials do not experience collisions in the high vacuum chamber, and therefore take a line-of-sight route from the source to the substrate. Mean free path (MFP), which is the measure of the length of collisionless transport of atoms, can be calculated from the average velocity $\bar{v}$ and time to collision t_{coll} as following:

$$\bar{v} = \sqrt{\frac{8RT}{\pi M}}, \tag{2.1}$$

$$t_{coll} = \frac{1}{\sqrt{2}\pi n d^2 \bar{v}}, \tag{2.2}$$

$$MFP = \bar{v} \cdot t_{coll} = \frac{1}{\sqrt{2}\pi n d^2} \tag{2.3}$$

where R =gas constant, n =number of moles, M =molecular weight, d =molecular diameter.

Since the number of moles proportional to the pressure of chamber $n \sim P$, thus:

$$MFP \sim 1/n \sim 1/P \tag{2.4}$$

The lower the chamber pressure, the higher the MFP and the better the formation and quality of the deposition. This ballistic flow of material from the source allows us to use the EBL as a resist mask to transfer the pattern we designed onto the substrate with high accuracy. In this thesis, all the material deposition is done by two high vacuum thermal evaporators: the Balzers evaporator used for depositing AlO_x has high vacuum (HV) condition of $\sim 10^{-5}$ mbar, and the Ultra-High Vacuum (UHV) evaporator used for depositing metals has a pressure of $\sim 10^{-8}$ mbar.

2.2 Sample Preparation

2.2.1 Fabrication Design

The two main parts of the sample are the SINIS junction and the coupling structure, both connected by the on-chip circuit, and connected to sample stage through bonding pads. It requires multiple steps of evaporation and oxidation, as well as a multi-layer design and fabrication. The standard electron beam lithography and deposition processes and equipment are used for the fabrication, with some slight modifications made for the specific requirements of our sample design. A standard EBL and PVD process is shown in the schematic in Fig. 2.1.

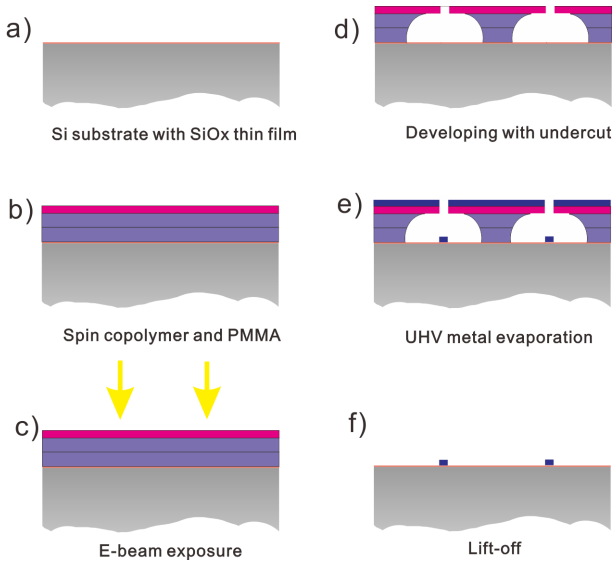

Figure 2.1: Schematic of a standard process of EBL and PVD process for metal wires deposition.

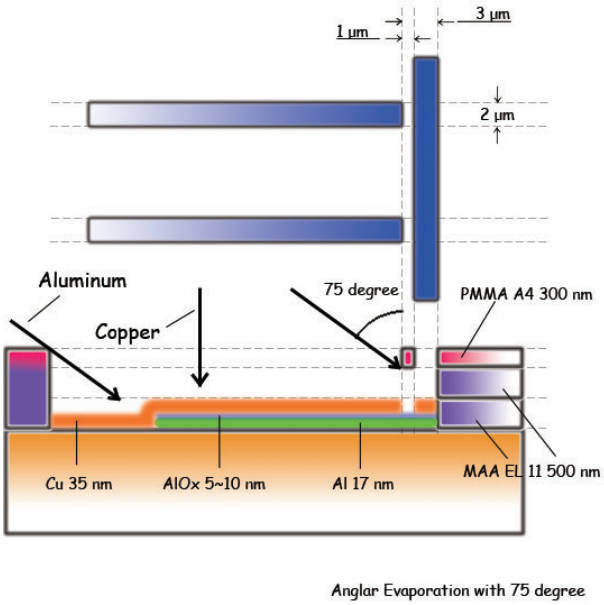

Figure 2.2: Schematic of the design of the SINIS junction. The upper figure is the top view and the lower figure is the cross section view of the SINIS structure.

The SINIS tunnel junction, which has Al-AlO_x-Cu-AlO_x-Al structure, is designed to be fabricated with conventional EBL and shadow evaporation techniques in a UHV chamber. The junction size was 1 μm^2, and the sample consists of a 17 nm thick Aluminium layer, a 35 nm thick copper layer and a thin thermal oxidized Al_2O_3 layer in between, as shown in Fig. 2.2.

The coupling structure consists of four niobium input washers with thickness 60 nm connected in series, and four output coils with thickness 120 nm, and two 200 nm thick AlO_x layers (total thickness 400nm) in between as insulation. As shown in Fig. 2.3, the square washer has an outer diameter 800 μm, hole side length 200 μm and a 10 μm gap; the output coils have 9 turns of 20 μm wide lines.

In the fabrication process, the SINIS junction should be fabricated after the coupling structure, due to it is vulnerability to further processing steps. Each coupling structure has three accurately aligned layers. The bottom and top layers are the Nb washer and output coil metal layers, in which the output coil has both bottom and top parts, and are connected through a open window in the middle layer. The middle AlO_x layer is used for isolating the two metal layers and carefully fabricated without pinholes.

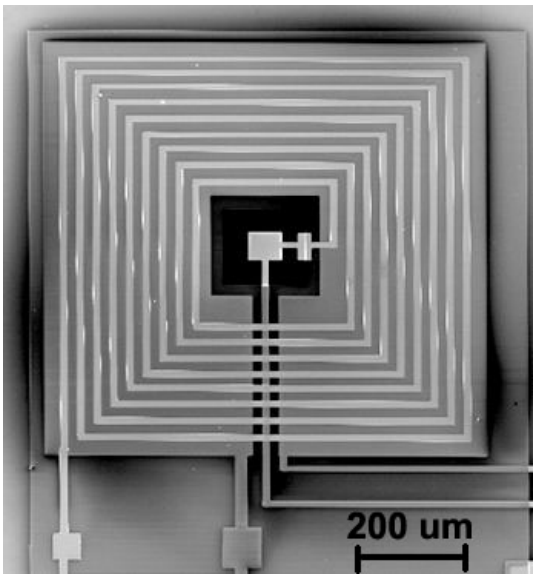

Figure 2.3: A scanning electron microscope picture of the sample washer and input coil structure.

There are four sets of alignment marks for this multi-layer fabrication process. One for rough alignment, two for accurate alignment of the middle and top coupling structure layers, and the last one for the SINIS junction alignment. All the sample patterns are designed using Elphy Quantum CAD software, the CAD design is shown in Fig. 2.4

2.2.2 Electron beam Resist

As shown in Fig. 2.2, the electron resists we used are polymethyl methacrylate 4% in anisole (PMMA A4), and copolymer methyl methacrylate and methacrylic acid P(MMA-MAA) 11% in ethyl lactate (EL 11). Two layers of copolymer EL 11 are first spun at 4000 rpm for 45 seconds for a thickness of approximately 500 nm and baked at 90 °C on hot plate for 60 seconds for each layer. Then one layer of PMMA A4 resist is spun at 2000 rpm for 45 seconds for a thickness of ∼300 nm and baked at the same temperature for 3 minutes.

In baking multiple layers, the total baking time should be considered for each layer, especially the bottom layer. Too long baking will result in burning the resists, and they become difficult to lift off. The bottom copolymer layer is more sensitive to electron beam exposure than the PMMA on top, and

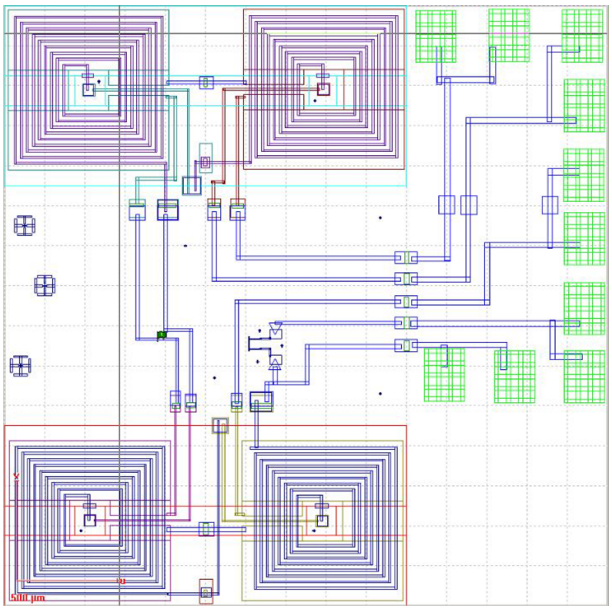

Figure 2.4: The CAD design of the sample in GDII CAD software.

forms wider area of soluble material in its layers. Thus, after development in MIBK, it will give a so-called undercut profile. The undercut is very important for fabricating SINIS junctions using the shadow evaporation technique used in this thesis, and it also helps to separate the deposited materials on the substrate from the ones on the upper PMMA mask resist layer, resulting in easy lift-off of the resist layer, and preventing the unwanted removal of the deposited materials on the substrate.

2.3 Sample Fabrication

The order of the sample fabrication processes is listed in the Table 2.3. Since many processes are repeated for different layers, we will discuss our sample fabrication according to the different processes used in this work in this section.

2.3.1 Electron Beam Lithography

All the electron beam exposures were done by the Raith e-LiNE 50 system as mentioned above. SINIS junctions were exposed at 20 kV acceleration voltage using an aperture of 30 μm and a dose of $\approx$140 μC/cm^2. The pattern design

Table 2.1: The order of the sample fabrication processes used in this work.

	Layer	Process
1	Washer, wiring, and alignment marks	EBL and 1st layer of Nb deposition in UHV
2	Insulator layer	EBL and 1st 200 nm of Al_2O_3 deposition in HV
3	Insulator layer	EBL and 2nd 200 nm of Al_2O_3 deposition in HV
4	Input coil and the connection between two metal layers	EBL and multi-angle Nb evaporation in UHV
5	SINIS junction	EBL, shadow evaporation technique in UHV

is shown in Fig. 2.4. Aperture and dosage for the coupling structures and the on-chip wiring leading to the bonding pads were 120 μm (the larger aperture gives a higher current and thus a shorter exposure time) and 140 $\mu C/cm^2$, respectively, with an acceleration voltage of 20 kV.

There are four exposures during the fabrication process due to the multilayer structure. For each layer except the first, the exposure begins with one rough alignment and one subsequently accurate alignment.

Each alignment requires the positions and relative positions of three different points on the substrate and the designed pattern. The computer will then calculate the angular, position and the magnification corrections for the sample in order to make it match the designed pattern. The original alignment marks are fabricated in the first exposure.

During the exposure of the insulation layer, in order to assure the continuous and pin-hole free quality of the deposited layer, several extra "patch" areas are exposed on the edges of the writing fields. These areas will receive overdose exposure, and result in expansion of the soluble areas of the resist layers after development. It is very important for the coupling structure, since pin-holes will form conduction channels or weak links between the metal layers and thus will tamper with the operation of the device.

2.3.2 Deposition

The deposition process takes place after the electron beam patterning and developing. In this thesis, the top and bottom layers of the coupling structure,

the SINIS junction and the connection wires and bonding pads are deposited in UHV, while the AlO_x insulation layer is deposited in HV (Balzer).

Niobium Deposition

The bottom Nb layer of coupling structure with all the connection wires, bonding pads, and alignment marks are first deposited to a thickness of 80 nm, using the conventional evaporation method. The evaporation direction is from the normal to the sample surface. The chamber pressure during the evaporation is $\approx 2.7 \times 10^{-8}$ mbar, the beam bias voltage is 10 KV and power is 2 kW. The deposition rate should be kept between 0.1 Å/s and 0.12 Å/s for the best film quality and coverage.

After the deposition of the first Nb layer, another 5 nm gold layer is immediately evaporated without breaking the vacuum with 2.5×10^{-8} mbar chamber pressure and 0.08 Å/s deposition rate. This Au layer is used as a protecting layer to prevent the oxidation of the Nb from air and the HV deposition process.

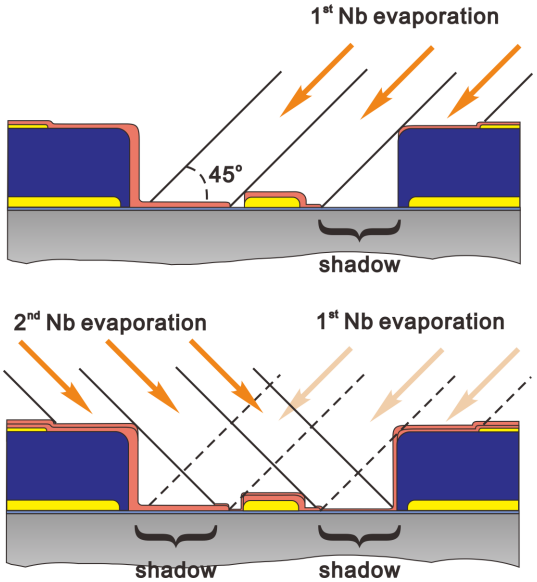

Figure 2.5: A schematic of the multi-angle Nb deposition process we used in the sample fabrication after the insulator deposition. In each time, the Nb layer is evaporated in two opposite directions for totally four times.

The bottom Nb layer and the middle insulation layer has a total thickness 500 nm, which requires an angular evaporation technique to ensure good step

coverage and thus good electronic contact through the connection hole. As shown in Fig. 2.5, there are two opposite sides of the connections that need to be deposited. First, one can tilt the sample stage bu 45°, and evaporate 40 nm of Nb, which will cover the wall of insulation layer and bottom niobium layer from one side, leaving the other side in a big shadow area. Then, the stage should turned to 45° angle from the opposite side, for a second 40 nm of Nb evaporation. This will make the contact for both sides. We do this for 4 times (with increasing evaporation thickness), and finish with one last 100 nm of Nb evaporation from the normal direction of the sample surface.

SINIS Junction Deposition

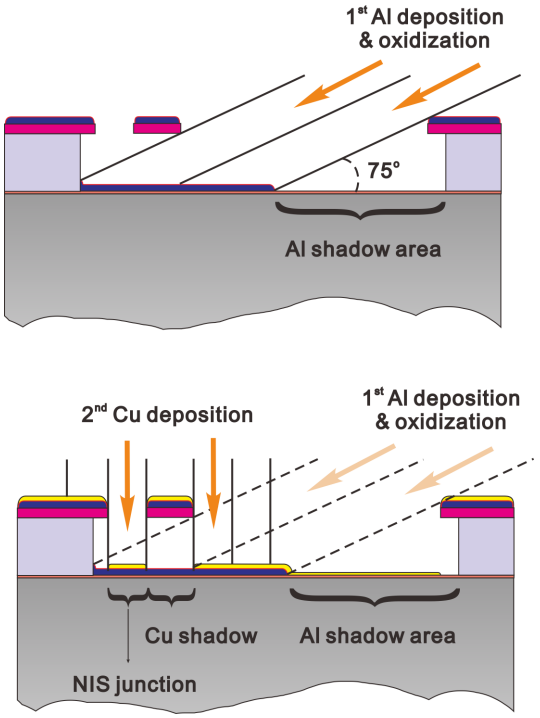

Figure 2.6: A schematic of the angular evaporation technique we used for the SINIS junction fabrication process.

The SINIS junction is fabricated by using the conventional shadow evaporation technique as shown in Fig. 2.6. First, a 17 nm Al layer is evaporated from a 75° angle to the normal of the sample surface. The chamber pressure is 2.5×10^{-8} mbar, the voltage is 2.1 KV and power is 10 kW. The deposition rate is kept at 0.5 Å/s-0.8 Å/s. Because there is a cavity under

the free-standing resist bridge, Al can reach the substrate paralleled to the evaporation angle, but leaves the perpendicular areas shadowed. Then, the sample stage is pulled back to the loading chamber, where the Al layer is oxidized in 40 mbar oxygen gas for 4 minutes to form a thin AlO_x layer. Last, a 35 nm Cu layer is evaporated normal to the substrate surface, with a chamber pressure 2.2×10^{-8} mbar and evaporation rate 0.2 Å/s. Cu will deposit onto all the open parts on the substrate, except where shadowed by the resist bridge, and thus forms two 1 μm overlap areas with Al as the tunnel junctions.

AlO_x Deposition

The insulation layer we used is AlO_x. It is evaporated from an Al_2O_3 crystal and we perform this process in another HV evaporator. The coverage, formation and quality of this AlO_x layer is key to our experiment. Therefore, we use a 10° tilt and a rotating sample stage for the evaporation. This method will give us much better coverage, pin-hole free layer and a smooth edge of the insulator layer. The evaporation is done at $\approx 4 \times 10^{-5}$ mbar chamber pressure with 0.2 Å/s evaporation rate for 200 nm each time, for a total of 400 nm.

2.4 General Fabrication Challenges

There are several processing challenges in this project.

First, the multi-layer fabrication requires an accurate alignment for each e-beam patterning steps. We use many sets of alignment marks for our sample fabrication. One set of rough alignment marks is designed on the edges of the pattern, and used for initially finding the sample structure and reducing the chance that we accidentally expose the structure area. Three sets of accurate marks are used after finishing the rough alignment with the writing field equal to the one that will be used for exposure. Each layer uses one set of accurate marks, since the used ones will be covered after each evaporation process, and thus hard to be focus onto during the future alignments.

Second, the electronic connection between the bottom layer and the top layer has to be considered carefully during the fabrication. The large thickness of the insulation layer wall makes the connection line between the bottom

and the top layer break easily. Therefore, we use the angle evaporation from opposite directions multiple times in order to get better coverage, and reduce the surface tension of the metal layers.

Third, as mentioned previously, the good quality of the insulation layer is very important. The chemical vapor deposition (CVD) and normal physical vapor deposition methods for a larger areas often leave some pin-holes, which will form unwanted connections between the metal layers. We use a rotating stage during the insulator evaporation to increase the quality and coverage of the AlO_x layer, and repeat the e-beam patterning and deposition process for this insulation layer for two times in order to minimize the effect from the resist residues.

The last difficulty is in the oxidation of the bottom Nb layer. During the processing, the bottom Nb is exposed to atmosphere and will slowly oxidize and cannot form good electronic connection with the top layer structure. This problem is normally solve by sputter cleaning before the second metal layer deposition. However, in our sample, if we want to evaporate the top layer after sputtering without breaking the vacuum, there is a big chance that we also induce defects and pin-holes to the insulation layer. We find that, if we evaporate a thin layer (8 nm) of Au immediately after the deposition of the bottom Nb layer, it will form a protective layer and give a good electronic contact to the top layer. A 8 nm Au layer can serve our purpose perfectly, and it is thin enough, so that the inverse proximity effect [54] will keep the whole structure still superconducting during the experiment, while it is also thick enough to prevent the Au atoms from forming discontinuous cluster structures.

Chapter 3

Preliminary Measurement

In our measurement setup, the samples are mounted on a low temperature stage of a ^{3}He-^{4}He dilution refrigerator, and are connected to the refrigerator's electronic by using Al bonding wires. The sample stage will be first cooled down to ∼50 mK, and then warmed up with certain temperature intervals until reached to 1 K in each measurement. The stage temperature is controlled by a metallic resistor which is biased with a PID controller through a variable resistor box with range from 100 Ω to 10 MΩ. The minimum heating power step is 100 pW. The stage temperature is measured by a RuO resistive thermometer with four probe method. We assume the temperature of the sample substrate equals to the temperature reading from the RuO thermometer since the good thermal conductivity of the Cu stage.

A DC-SQUID is mounted at the 1.5 K stage. In the final measurement, the sample signal comes from the input inductor on the sample stage through superconducting wires, and is magnetically coupled to the main SQUID junctions, then picked up and amplified by using the flux lock technique. The SQUID we used is a two stage DC SQUID amplifier fabricated at NIST Boulder, which is connect to the sample stage with superconducting Nb-Ti wires and superconducting Al bonding wires on the sample substrate. The detail about the SQUID we used can be found in Ref. [55], and the schematic of this SQUID is shown in Fig. 3.1.

There are three main measurements we performed in this work, the details of the signal sources and experiment setups for each measurement will be introduced in the following sections. All the measured signals are acquired by a NI-DAQmx module on the PXI platform from National Instrument with 20 kHz sampling rate, and transferred to the measurement computer through

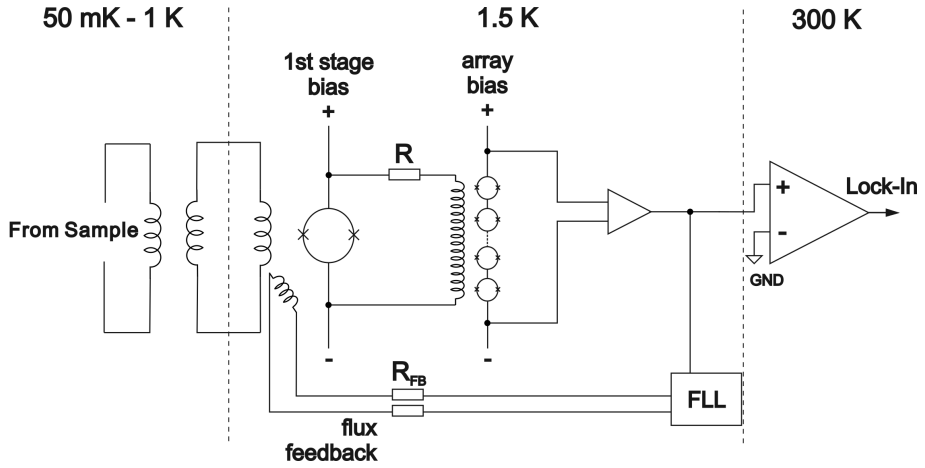

Figure 3.1: The schematic of the two stages SQUID used in our work [55]. The SQUID is mounted on the 1.5 K stage, and connects to the sample stage by using Nb-Ti wires. One lock-in amplifier is used at room temperature to readout the SQUID signal.

the electronic isolated optical wires. The measurement data are recorded by a self-made Labview program, except the spectrum analyzer data, which is stored on floppy disks.

3.1 SINIS Junction Measurement with DC Bias

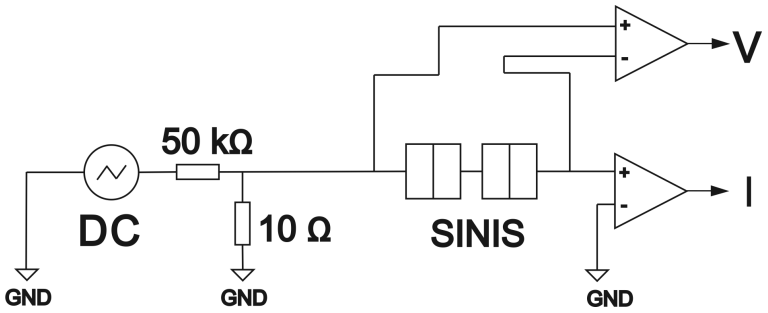

Figure 3.2: The schematic of the DC measurement setup. A self-made sweeping battery box is used as DC source, and the I-V characteristic of the sample is measured by two pre-amplifier.

The first measurements were performed to determine the DC characteristics of the SINIS junction we used in the experiment. In the experiment,

the SINIS I-V characteristics is measured by measuring the sample bias voltage and the current response. A sweeping DC source with output voltage ranging from -4 V to 4 V is used with sweep time of 1770 s and a 1/5000 voltage divider to reduce the voltage. The measurement is done by a voltage pre-amplifier (ITHACO Model 1201) with low pass filter at 3 Hz for measuring the bias voltage, and a current pre-amplifier (ITHACO Model 1211) with integration time of 300 ms for measuring the current response from the sample. The schematic of this measurement setup is shown in Fig. 3.2.

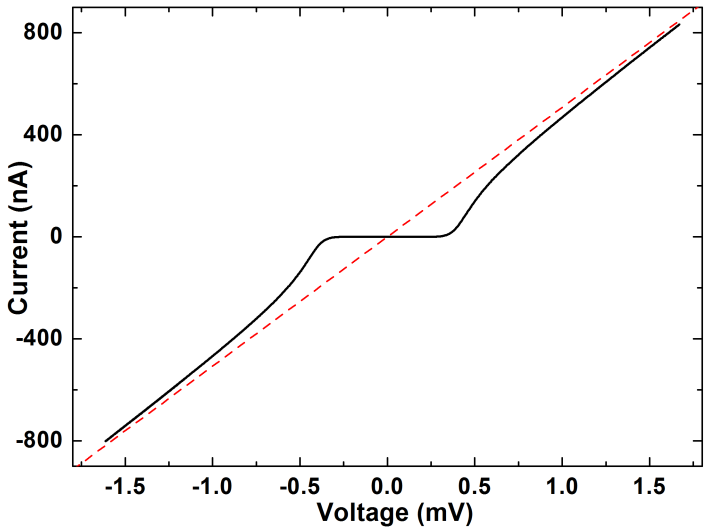

Figure 3.3: The SINIS junction I-V characteristic from a DC measurement at 60 mK. The solid line is the measured data and the red dashed line represents the ohmic behavior of a 2 kΩ resistor.

First, the stage temperature is kept at 60 mK. The I-V characteristic of the SINIS junction at this temperature is measured and shown in Fig. 3.3. At higher voltages, the junction resistance approaches to a simple constant resistive behavior indicated by the dashed red line, which gives the tunneling conductance G_N. But at voltages lower than ± 0.5 mV, the junction current begins to decrease and reaches around 0 at ~ 0.44 mV, which indicates the value of the superconducting energy gap.

In Fig. 3.4 we show a derivative plot of the current with respect to voltage against the bias voltage. This figure gives us the junction differential conductance changes as a function of the applied voltage, and we can easily use this data to calculate the superconducting gap $2\Delta = 0.44$ mV of the Al film and the tunneling resistance $R_T = 1/G_N = 2010\Omega$ of the junctions

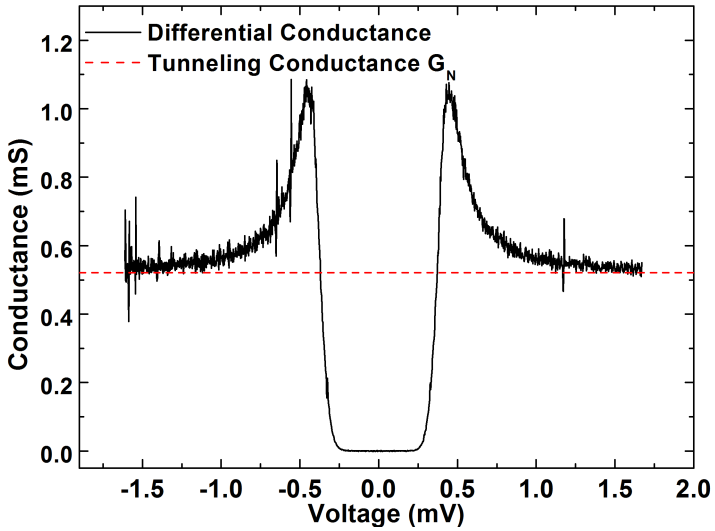

Figure 3.4: The SINIS junction dI/dV characteristic for the DC measurement at 60 mK. The solid line is the derivative of the measured current data against voltage, and the red dashed line represents the ohmic behavior with resistance $R_T = 1/G_N = 2$ kΩ.

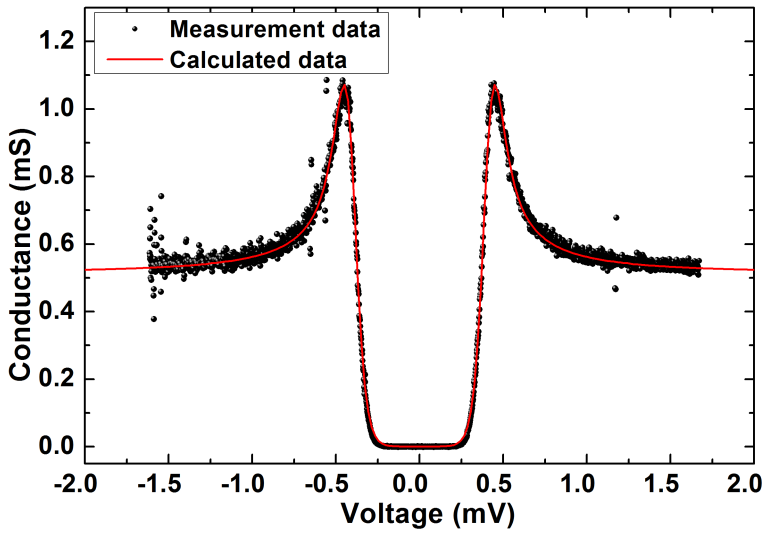

Figure 3.5: A comparison between the DC measurement data, shown as black dots, and the calculated BCS theory curve, shown as red solid line at 60 mK.

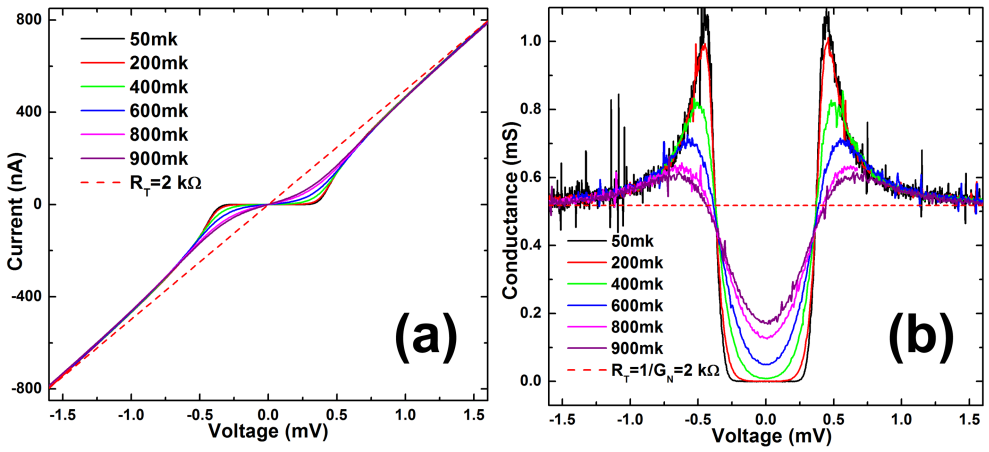

Figure 3.6: The SINIS junction (a)I-V characteristics and (b) differential conductance plots at different stage temperatures. The solid lines are the measured data, and the red dashed line represents the ohmic behavior with resistance $R_T = 1/G_N = 2$ kΩ.

shown as the dashed red line. These two parameters we acquired can be used for calculating the BCS theory curve and comparing it with the measured data as shown in fig. 3.5. It can be seen that the data is in good agreement with BCS theory in general.

Fig. 3.6 shows the SINIS junction I-V characteristics and its calculated differential conductance plots at different stage temperatures. We can see from this data that at a higher stage temperature, the SINIS device begins to have a more resistive behavior resembling more a pure resistor. The sharp output of current at the Al energy gap is also smeared. This behavior is predicated by the theory we discussed in the Chapter 1.2 (Equation. 1.23), and it is the key feature for the SINIS junction thermometry.

3.2 Impedance and SQUID Noise measurement

The purpose of measuring the impedance and noise of the system is to find a feasible source frequency regime for the AC bias measurement, which has comparatively lower system noise level and a minimal influence coming from SQUID electronics. The frequency dependent complex impedance and sample noise are measured by a lock-in amplifier and a spectrum analyzer (Agi-

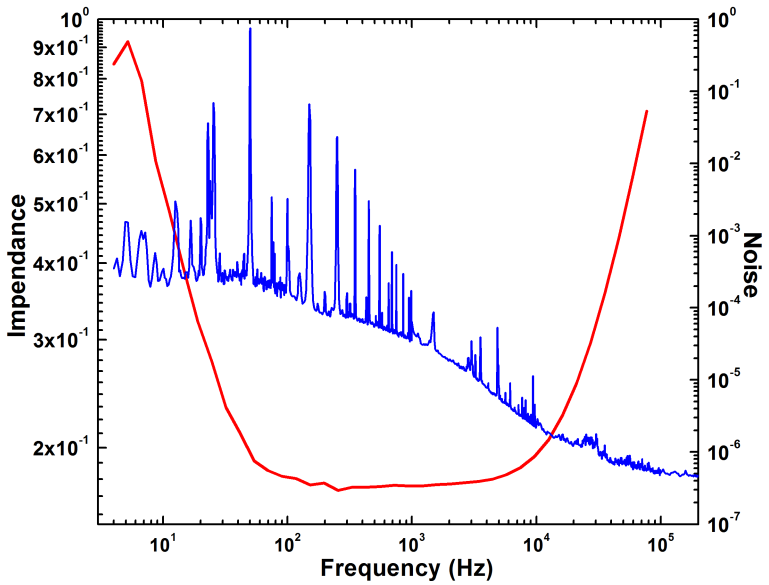

Figure 3.7: A comparison between the frequency dependent impedance and the noise of the system. The blue line is the system noise level, the red line is the impedance.

lent 89410A Vector Signal Analyzer) respectively. In the this measurement, the lock-in amplifier is used to generate a reference signal of sweeping frequency to the sample, with the current response measured from the SQUID output. In the noise measurement, the spectrum analyzer is directly connected to the SQUID output, and measures the noise which is generated by the SQUID electronics and the sample.

As shown in Fig. 3.7, the blue line represents the system noise spectrum. It has a higher noise level at low frequency regime $\sim$ 50 Hz-1 kHz. Many interference peaks are also observed mainly at 50 Hz and its harmonic frequencies, which come from the power lines. The noise diminishes at higher frequencies ($>$ 1 kHz) as shown in the figure, but the same time the cut off from impendence of the SQUID electronics begins to dominate and attenuates the sample signal above 10 kHz. The measured impedance changes against the frequency is shown by the red line. From Fig. 3.7, we find that at frequency around 26 kHz, there is a regime that has a lowered system noise level as well as still low impedance, and this is the frequency we want to use in our AC bias measurement to get the best possible results.

It is important to note that this is a very preliminary measurement, there are neither filters used in the cryostat nor the shunt resistor in the super-

conducting loops to help with interference pickup, and the measurement frequency is also limited by the Lock-in amplifier up to 100 kHz. The setup will require more careful optimization and impedance matching, and this will be done works in the future.

3.3 Sample Measurement with AC Bias

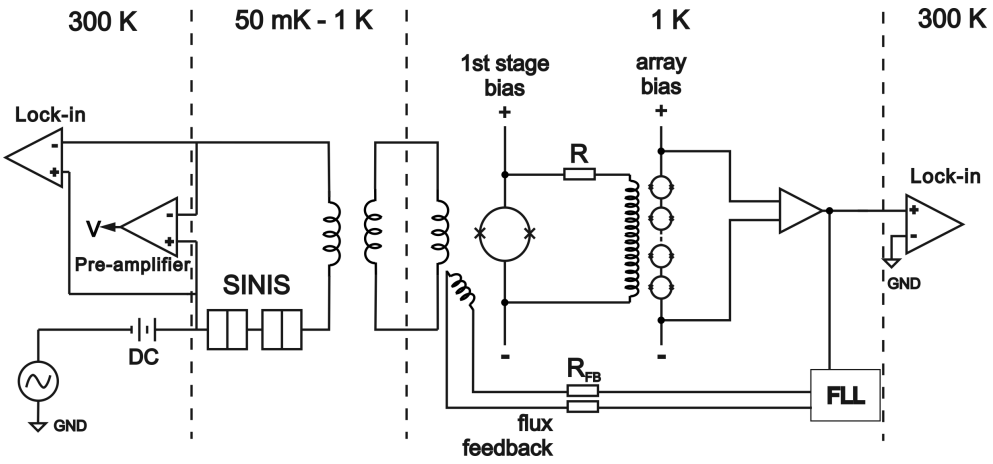

Figure 3.8: The schematic of the AC measurement setup. The AC signal is generated by one lock-in amplifier and the slow sweeping DC voltage is generated by a self-made battery box. Two lock-in amplifiers are used to measure the conductance of the sample, and one voltage pre-amplifier is used to measure the DC voltage bias of the SINIS device.

In the AC characteristics measurements, the conductance of the SINIS junction is measured based on the four probe technique by measuring the locked-in AC voltage response directly from sample output, and measuring the current response through the coupling structure of the sample by a SQUID. The DC voltage bias of the sample is also measured in this experiment. In the measurement setup, one voltage pre-amplifier with the same setting as in the DC measurement and two lock-in amplifiers (Stanford Research Systems SR830) are used. The reference AC signal is generated from one lock-in amplifier with 26 KHz reference frequency and 100 mV bias, and connected in series to a slowly sweeping DC source with the same settings as in DC measurement. The DC and AC voltages are summed and form a sine signal with a slow sweeping DC level offset. The DC voltage bias level is directly measured by the voltage pre-amplifier. The current response signals

from SQUID output and the DC voltage response signals from the sample output are measured by lock-in amplifiers at the reference frequency. The schematic of this measurement setup is shown in Fig. 3.8, and the sample was measured with the same temperature sets as in the DC measurement.

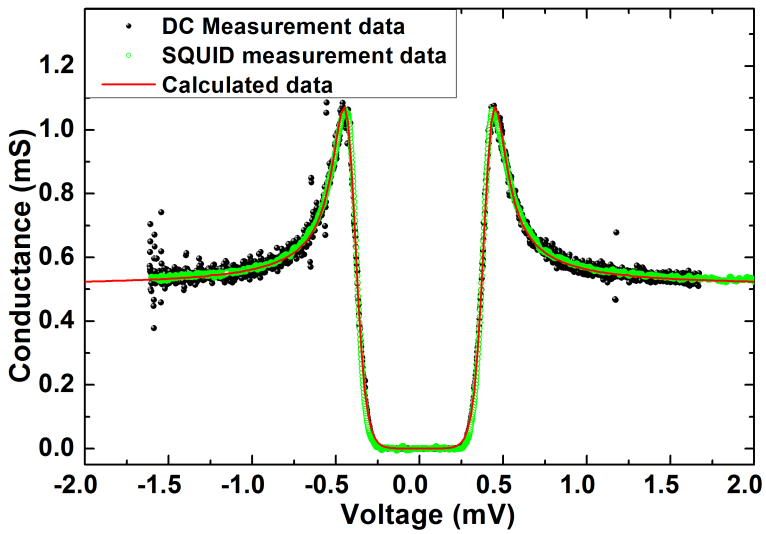

Figure 3.9: A comparison between the SQUID measurement data, shown as green open circles, and the calculated BCS theory curve, shown as red solid line at 60 mK. The DC measurement data at 60 mK are also shown in this figure as black dots.

In the Fig. 3.9, we compare the conductance $G(V)$ of our SQUID measurement data at 60 mK (green circle) with the calculated conductance of the DC measurement data (black dot) and the calculated data from BCS theory (red line) which already shown in Fig. 3.5. And in Fig. 3.10, we show the conductance $G(V)$ from both the standard DC measurements and the SQUID measurements at four different bath temperatures between 50 mK and 1 K. The solid lines in Fig. 3.10 are the calculated conductance curves from DC measurement (numerical differentiation) and the open circles are the SQUID measurement results. The SQUID measurement results are in good agreement with the BCS theory curve at 60 mK, and follow extremely well the DC results for all temperatures we measured. They share the same Al film energy gap Δ and tunneling resistance R_T, showing that our measurement scheme works. The inset (b) in Fig. 3.10 shows the same conductance data from 0.1 mV to 0.6 mV, in which range, the conductance of the junction is more sensitive to the temperature changes, and it is the functional regime

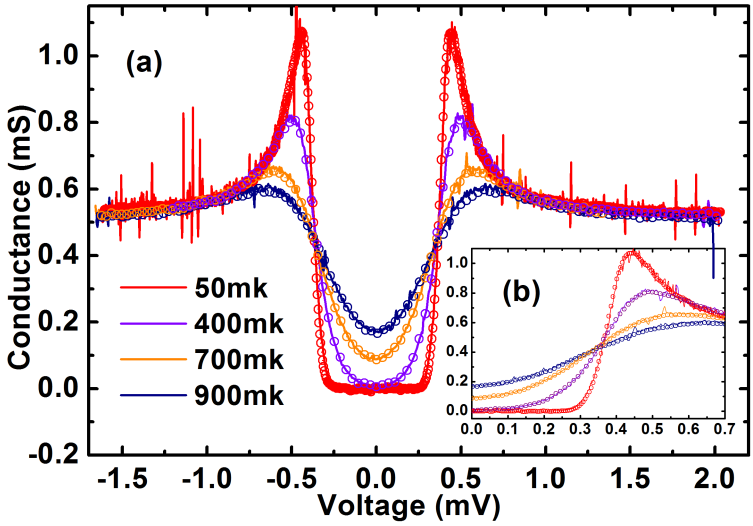

Figure 3.10: The temperature dependence of SINIS tunnel junction conductance $G(T)$ with varying bath temperature from 50 mK to 1 K from the SQUID and DC measurements. Different curves correspond to different bath temperatures. Open circles: SQUID measurement, lines: DC measurement. Inset: Zoom-in at the useful range.

for our thermometry.

Figure 3.11 gives the temperature dependence of the SINIS tunnel junction conductance $G(T)$ from 50 mK to 1 K with different voltage biases from the SQUID measurement. An interesting observation is that there is a strongly temperature-dependent regime below $T < 0.2$ K with opposite responsivity (G increasing with T rather than decreasing as observed at $T > 0.2$ K) when the bias voltage is near the superconductor energy gap Δ. This behavior is confirmed by the BCS theory simulation shown in Fig. 3.12, namely, that at the bias voltage below and close to the energy gap, there is a sharp change for the temperature dependence of the conductance.

Generally, the responsivity is one important parameter to characterize a thermometer. For a normal current biased SINIS junction thermometer, the responsivity, S_V, is described by the voltage response to the change of temperature

$$S_V = \frac{\delta V}{\delta T}. \tag{3.1}$$

And it is also important to point out that the responsivity of a thermometer is part of the responsivity of a bolometer S_{VP}

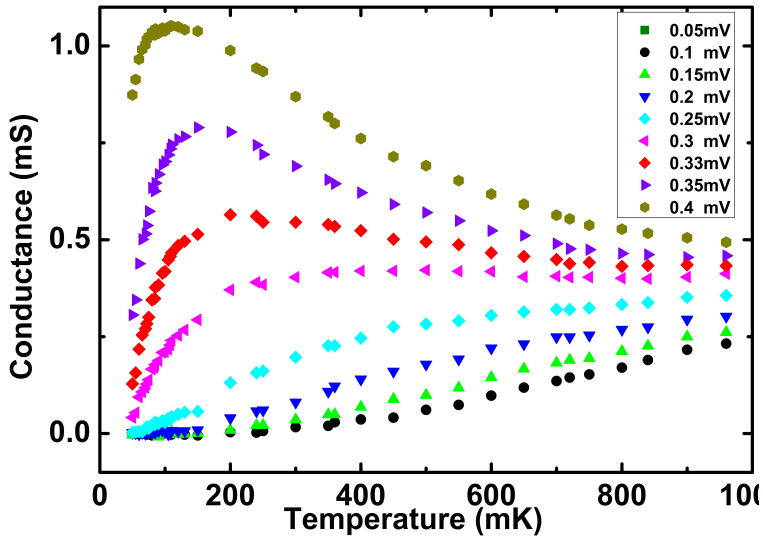

Figure 3.11: $G(T)$ from the SQUID measurement. Different colors correspond to different bias voltages between 0.05 mV to 0.4 mV. 2Δ is approximately 0.45 mV.

$$S_{VP} = \frac{\delta V}{\delta P} = \frac{\delta V}{\delta T}\frac{\delta T}{\delta P}. \tag{3.2}$$

The V-T curve of our sample from DC measurement with 100 pA bias is shown in Fig. 3.13, the said responsivity S_V is about 0.5 μV/mK at 100 mK. In our measurement, if we assume the amplitude of the biased AC signal is kept constant (which can be realized by increase the tunneling resistance R_T of the SINIS junction), the effective responsivity of our SQUID measurement with 0.35 mV DC bias at 100 mK at the SQUID output is around 2.7 μV/mK. Therefore, we believe this part can be used as a very sensitive thermometer at temperatures lower than $\sim$ 0.2 K. We stress that this responsivity is still good at our base temperature 50 mK, especially considering that no filters were used in the measurement wires. In contrast, in the higher temperature regime (from 200 mK to 1 K), a lower bias voltage will give a higher $G(T)$ sensitivity to the temperature, and thus one should choose the bias value based on the required temperature range.

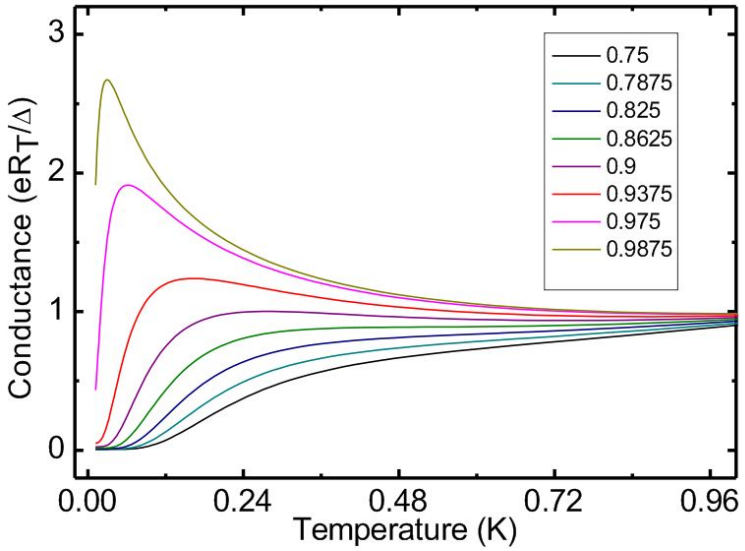

Figure 3.12: $G(T)$ Computer simulation for the temperature dependence of conductance G(T) based on BCS theory. Different colors represent different voltage bias (in unit of Δ).

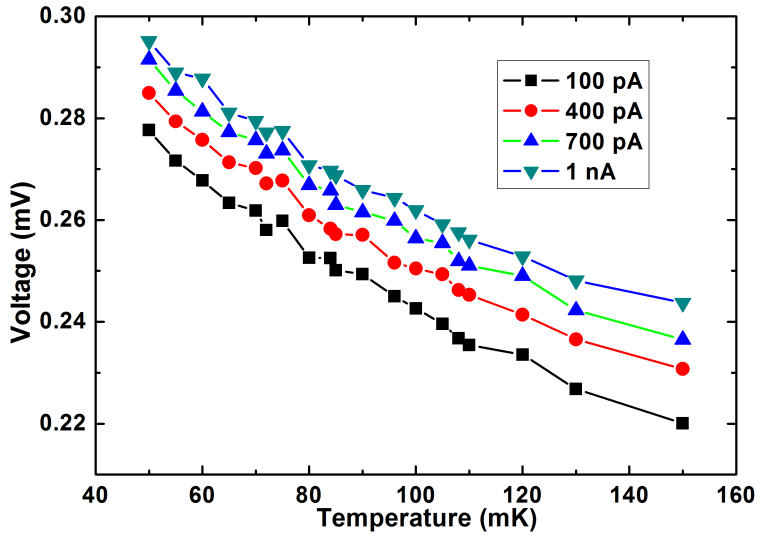

Figure 3.13: The temperature dependent of voltage response of our sample with four different current biases in the temperature range between 50 mK to 150 mK.

Chapter 4

Conclusions

The goals of this project were to develop, fabricate and test the feasibility of comparatively fast SQUID read out of a SINIS thermometer, using a inductive coupling structure integrated on the sample substrate. The sample design and fabrication were crucial for this project due to the multilayer structure. We met many problems during the sample processing, such as pin-holes in the insulator layer, oxidization of the bottom niobium layer, and bad contact between the top and bottom metal layer. Modifications were made to solve these problems to ensure the quality of the sample, and we succeeded in fabricating a working sample used in this thesis.

Two measurements were performed on our sample, one with a normal DC measurement setup, and the other with a AC bias and SQUID read-out setup. Our data indicates that the SQUID measurement follows well the DC bias measurement and the BCS theory for the SINIS junction, and shows that it is feasible to use this scheme to directly measure the conductance of a SINIS device at audio frequencies. The frequency of operation of this type of device is not limited to audio frequency range, but could possibly be extended to RF (up to few MHz), where limitations of SQUID amplifier and SINIS internal thermal time constants are met. We have a plan for a new sample, which is more carefully designed and optimized and operated at higher frequency in the future.

Bibliography

[1] D. Schmidt. Nanoscale radio-frequency thermometry. *Appl. Phys. Lett.*, 83(5):1002, 2003.

[2] D. R. Schmidt. A superconductor-insulator-normal metal bolometer with microwave readout suitable for large-format arrays. *Appl. Phys. Lett.*, 86(5):053505, 2005.

[3] D. Chouvaev, L. Kuzmin, and M. Tarasov. Normal-metal hot-electron microbolometer with on-chip protection by tunnel junctions. *Superconductor Science and Technology*, 12(11):985–988, 1999.

[4] J. M. Kivioja, I. J. Maasilta, J. P. Pekola, and J. T. Karvonen. Response time of a thermometer based on normal metal-insulator-superconductor (nis) tunnel junctions. *Physica E: Low-dimensional Systems and Nanostructures*, 18(1-3):21–22, 2003.

[5] J. T. Karvonen and I. J. Maasilta. Influence of phonon dimensionality on electron energy relaxation. *Physical Review Letters*, 99(14):145503, 2007.

[6] P. J. Koppinen and I. J. Maasilta. Phonon cooling of nanomechanical beams with tunnel junctions. *Physical Review Letters*, 102(16):165502, 2009.

[7] M. Meschke, W. Guichard, and J. P. Pekola. Single-mode heat conduction by photons. *Nature*, 444(7116):187–90, 2006.

[8] D. R. Schmidt, W. D. Duncan, K. D. Irwin, K. W. Lehnert, N. A. Miller, and J. N. Ullom. Normal metal-insulator-superconductor junction technology for bolometers. *Nuclear Instruments and Methods in Physics Research Section a-Accelerators Spectrometers Detectors and Associated Equipment*, 559(2):516–518, 2006.

[9] F. Giazotto, T. T. Heikkila, A. Luukanen, A. M. Savin, and J. P. Pekola. Opportunities for mesoscopics in thermometry and refrigeration: Physics and applications. *Reviews of Modern Physics*, 78(1):217–274, 2006.

[10] H. K. Onnes. The resistance of pure mercury at helium temperatures. *Proceedings of the Koninklijke Nederlandse Akademie Van Wetenschappen*, 100(3-4):153–155, 1911.

[11] H. K. Onnes. On the sudden change in the rate at which the resistance of mercury disappears. *Proceedings of the Koninklijke Nederlandse Akademie Van Wetenschappen*, 100(3-4):158–+, 1911.

[12] H. K. Onnes. The disappearance of the resistance of mercury. *Proceedings of the Koninklijke Nederlandse Akademie Van Wetenschappen*, 100(3-4):156–158, 1911.

[13] W. Meissner and R. Ochsenfeld. Ein neuer effekt bei eintritt der supraleitfähigkeit. *Naturwissenschaften*, 21(44):787–788, 1933.

[14] Terry P. Orlando and Kevin A. Delin. *Foundations of applied superconductivity*. Addison-Wesley, 1991.

[15] F. London. On the problem of the molecular theory of superconductivity. *Physical Review*, 74(5):562, 1948.

[16] J. Bardeen, L. N. Cooper, and J. R. Schrieffer. Microscopic theory of superconductivity. *Physical Review*, 106(1):162, 1957.

[17] J. G. Bednorz and K. A. Müller. Possible high tc superconductivity in the ba-la-cu-o system. *Zeitschrift für Physik B Condensed Matter*, 64(2):189–193, 1986.

[18] V. Ginzburg. On the theory of superconductivity. *Il Nuovo Cimento (1955-1965)*, 2(6):1234–1250, 1955.

[19] J. Bardeen, L. N. Cooper, and J. R. Schrieffer. Theory of superconductivity. *Physical Review*, 108(5):1175–1204, 1957.

[20] Bernhard Mühlschlegel. Die thermodynamischen funktionen des supraleiters. *Zeitschrift für Physik A Hadrons and Nuclei*, 155(3):313–327, 1959.

[21] Michael Tinkham. *Introduction to superconductivity*. International series in pure and applied physics. McGraw Hill, 2nd edition, 1996.

[22] J. C. Fisher and I. Giaever. Tunneling through thin insulating layers. *Journal of Applied Physics*, 32(2):172, 1961.

[23] I. Giaever and K. Megerle. Study of superconductors by electron tunneling. *Physical Review*, 122(4):1101, 1961.

[24] R. C. Dynes, V. Narayanamurti, and J. P. Garno. Direct measurement of quasiparticle-lifetime broadening in a strong-coupled superconductor. *Physical Review Letters*, 41(21):1509, 1978.

[25] R. C. Dynes, J. P. Garno, G. B. Hertel, and T. P. Orlando. Tunneling study of superconductivity near the metal-insulator transition. *Physical Review Letters*, 53(25):2437, 1984.

[26] J. P. Pekola, Heikkil, auml, T. T., A. M. Savin, J. T. Flyktman, F. Giazotto, and F. W. J. Hekking. Limitations in cooling electrons using normal-metal-superconductor tunnel junctions. *Physical Review Letters*, 92(5):056804, 2004.

[27] B. D. Josephson. Possible new effects in superconductive tunnelling. *Physics Letters*, 1(7):251–253, 1962.

[28] Vinay Ambegaokar and Alexis Baratoff. Tunneling between superconductors. *Physical Review Letters*, 10(11):486, 1963.

[29] J. M. Rowell and D. C. Tsui. Hot electron temperature in inas measured by tunneling. *Physical Review B*, 14(6):2456, 1976.

[30] M. Nahum, T. M. Eiles, and John M. Martinis. Electronic microrefrigerator based on a normal-insulator-superconductor tunnel junction. *Applied Physics Letters*, 65(24):3123–3125, 1994.

[31] M. Nahum and John M. Martinis. Ultrasensitive-hot-electron microbolometer. *Applied Physics Letters*, 63(22):3075–3077, 1993.

[32] J. Mees, M. Nahum, and P. L. Richards. New designs for antenna-coupled superconducting bolometers. *Applied Physics Letters*, 59(18):2329–2331, 1991.

[33] M. M. Leivo, J. P. Pekola, and D. V. Averin. Efficient peltier refrigeration by a pair of normal metal/insulator/superconductor junctions. *Applied Physics Letters*, 68(14):1996–1998, 1996.

[34] Dragos-Victor Anghel and Leonid Kuzmin. Capacitively coupled hot-electron nanobolometer as far-infrared photon counter. *Applied Physics Letters*, 82(2):293–295, 2003.

[35] S. Chaudhuri and I. J. Maasilta. Cooling, conductance and thermometric performance of non-ideal normal metal-superconductor tunnel junction pairs. *arXiv:1112.0197*, 2011.

[36] Range and Shannon K'doah. Gravity probe b: Exploring einstein's universe with gyroscopes. *NASA*, 2004.

[37] J. Clarke and A. I. Braginski. *The SQUID handbook*. Wiley-VCH, 2004.

[38] R. L. Fagaly. Superconducting quantum interference device instruments and applications. *Review of Scientific Instruments*, 77(10), 2006.

[39] J. M. Jaycox and M. B. Ketchen. Planar coupling scheme for ultra low-noise dc squids. *Ieee Transactions on Magnetics*, 17(1):400–403, 1981.

[40] M. B. Ketchen. Design considerations for dc squids fabricated in deep submicron technology. *Ieee Transactions on Magnetics*, 27(2):2916–2919, 1991.

[41] W. Chang. The inductance of a superconducting strip transmission line. *J. Appl. Phys.*, 50(12):8129, 1979.

[42] A. I. Gubin, K. S. Il'n, S. A. Vitusevich, M. Siegel, and N. Klein. Dependence of magnetic penetration depth on the thickness of superconducting nb thin films. *Physical Review B*, 72(6):064503, 2005.

[43] Simon Reif-Acherman. Heike kamerlingh onnes: Master of experimental technique and quantitative research. *Physics in Perspective (PIP)*, 6(2):197–223, 2004.

[44] Kühlwein Ludwig. Helium recovery: Tailor-made and absolutely gastight. *Bauer Compressors News*, 2007.

[45] L. T. Aldrich and Alfred O. Nier. The occurrence of he^3 in natural sources of helium. *Physical Review*, 74(11):1590, 1948.

[46] Frank Pobell. *Matter and methods at low temperatures*. Springer, 3rd, rev. and expanded edition, 2007.

[47] D. S. Betts. *Refrigeration and thermometry below one Kelvin*. Graduate student series in physics. Sussex University Press, 1976.

[48] G. Frossati. Experimental techniques: Methods for cooling below 300 mk. *Journal of Low Temperature Physics*, 87(3):595–633, 1992.

[49] J. Wilks and D. S. Betts. *An introduction to liquid helium*. Clarendon Press ; Oxford University Press, 2nd edition, 1987.

[50] Dennis S. Greywall. ^{3}he specific heat and thermometry at millikelvin temperatures. *Physical Review B*, 33(11):7520, 1986.

[51] G. E. Watson, J. D. Reppy, and R. C. Richardson. Low-temperature density and solubility of he^3 in liquid he^4 under pressure. *Physical Review*, 188(1):384, 1969.

[52] J. P. Pekola, J. M. Kyynarainen, M. M. Leivo, and A. J. Manninen. Nis chip refrigeration. *Cryogenics*, 39(8):653–657, 1999.

[53] Sami Franssila. *Introduction to microfabrication*. J. Wiley, 2004.

[54] W. Silvert. Theory of superconducting proximity effect. *Journal of Low Temperature Physics*, 20(5-6):439–477, 1975.

[55] J. A. Chervenak, K. D. Irwin, E. N. Grossman, J. M. Martinis, C. D. Reintsema, and M. E. Huber. Superconducting multiplexer for arrays of transition edge sensors. *Applied Physics Letters*, 74(26):4043–4045, 1999.

Appendix

A Raith e-LiNE

General Information

- Electron beam lithography: min. feature size < 20 nm
- High resolution SEM imaging: resolution < 10 nm

Key Specifications:

Property	Measured	Factory Spec
Filament	Schottky TFE	
Beam size	1.8nm @ 20 keV	2nm @ 20 keV
	3.5 nm @ 1 keV	4 nm @ 1 keV
Beam current range	5 pA - 20 nA	
Beam energy	100 eV - 30 keV	
Current stability	< 1.2 % in 11 h	max. 0.5 %/h
Min. feature size	18.2 nm line	20 nm
Min. grating periodicity	73 nm (32.4 nm line)	100 nm (50 nm line)
Stitching accuracy (100 μm write field, 10 keV)	mean $+3\sigma = 36$ nm	mean $+3\sigma < 60$ nm
Overlay accuracy	mean $+3\sigma = 39$ nm	mean $+3\sigma < 40$ nm
z sensing reproducibility	0.74 μm	< 1 μm

Key Features

- TFE gun
- Cross over free beam path
- High beam current density

- Compound objective lens for lowest beam aberrations
- Digital controlled electron optics column
- Fast electrostatic beam blanking
- 45 mm laser interferometer stage
- True closed loop piezo control for finest sample position
- 2 nm XY position resolution at any WD, WF size and SEM magn
- WFs from 0.5 μm to 2 mm with automated calibration and selection
- 10 MHz DSP controlled high speed
- Pattern processor
- System control software
- Multi user interface
- SEM inspection software
- Image archiving software
- Dimensional metrology software
- Integrated GDSII editor
- Proximity effect correction
- Data post-processor

B UHV Evaporator

Ultra High Vacuum (UHV) evaporator supplied by Instrumentti Mattila; manufactured and installed 1998.

System includes:

- E-gun, Telemark TT 10
- Cryopump, Cryo-torr 8

- Ion Gun, Tectra IonEtch GenII

Materials evaporated: Au, Ag, Ti, Nb, Ta, Cu, Al, Bi, V, Ge, Pt, Sn, Pd, Mo, Si. 6 materials can be in the chamber at a time.

C RIE/CVD

Oxford Instruments Plasmalab 80plus

Combined instrument for reactive ion etching (RIE), plasma etching (PE) or plasma enhanced chemical vapor deposition (PECVD).

Property	Value
Wafer size	Up to 7 x 2", 4 x 3", 2 x 4" or one 6" or 8"
Substrate temperature	-150 °C to +400 °C

Available gases: Ar, O_2, SF_6 and CHF_3